Analysis and Optimal Modulation for 2/3-Level DAB Converters to Minimize Current Stress With Five-Level Control

Song, Chaochao; Sangwongwanich, Ariya; Yang, Yongheng; Pan, Yiwei; Blaabjerg, Frede

Published in:
I E E E Transactions on Power Electronics

DOI (link to publication from Publisher):
10.1109/TPEL.2023.3235938

Publication date:
2023

Document Version
Accepted author manuscript, peer reviewed version

Analysis and Optimal Modulation for 2/3-Level DAB Converters to Minimize Current Stress With Five-Level Control

Chaochao Song, *Student Member, IEEE,* Ariya Sangwongwanich, *Member, IEEE,* Yongheng Yang, *Senior Member, IEEE,* Yiwei Pan, *Student Member, IEEE,* and Frede Blaabjerg, *Fellow, IEEE*

***Abstract*—Two-three (2/3)-level dual-active-bridge (DAB) DC-DC converter has high potential to become a promising solution for medium-voltage high-power applications. However, its switching characteristics, modeling, and optimal modulation schemes have not been comprehensively explored yet. In order to avoid voltage and current distortions, and ensure reliable operation, this paper analyzes the operating constraints for the neutral-point-clamped (NPC)-based DAB converters. Based on the obtained operating constraints, the transferred power and current stress models under a five-level control scheme, which is considered as one of the most advantageous control strategies for the NPC-based DAB converters, are obtained with an equivalent-wave modeling method. Generic control strategies based on analytical solutions have not be fully explored for the multi-level DAB converters due to the increased number of control variables. With the above, this paper proposes a minimum-current-stress control strategy employing analytical solutions in the entire power range, which are obtained by combining the Karush-Kuhn-Tucker (KKT) conditions and numerical-solution analysis. With the proposed modulation scheme, the control variables can be automatically modified online, instead of relying on offline calculation of the numerical control variables. Therefore, the control complexity can be reduced significantly, especially when the operating parameters change in a wide range. Finally, experimental tests verify the effectiveness of the analysis.**

***Index Terms*—Multi-level DAB converters, modeling, current stress, optimal modulation, efficiency.**

I. Introduction

DUAL-active-bridge (DAB) DC-DC converters were originally proposed in the 1990s for high-power-density applications [1]. Due to the advantages including galvanic isolation, inherent soft-switching capability, and high efficiency, the DAB converters have been widely used in the past decades [2], [3]. Tailor-made for various applications like energy storage systems, distributed generation, and solid-state transformers, different structures have been developed including three-phase, current-fed, and multi-level DAB converters [4]–[9]. Recently, due to the development of the medium-voltage semiconductors, e.g., 3.3 kV and 6.5 kV MOSFET, multi-level DAB converters, which are suitably applied to the medium-voltage DC (MVDC) systems with DC bus voltage of several thousand volts, e.g., large-scale photovoltaic (PV) plants as shown in Fig. 1, have drawn more and more attention [10]–[15]. Specially, a two-three (2/3)-level DAB converter, as shown in Fig. 2, was proposed for the applications where the input and output voltage ratings are considerably different [6], [7]. A 2/3-level DAB converter is composed of a two-level H-bridge at the primary side and a three-level neutral-point-clamped (NPC) bridge at the secondary side. Compared to the two-level DAB converter, the 2/3-level DAB converter can achieve higher voltage blocking capability and step-up ratios to improve the conversion efficiency. Moreover, it can also provide more degrees of freedom (DoFs) to improve the performance of the DAB converters, e.g., efficiency [8], [9]. In addition, compared to the cascaded converters which can also be applied to MVDC systems, e.g., input-parallel-output-series (IPOS) converter based on two-level DAB converters, the single 2/3-level DAB converter can reduce the devices such as semiconductors and transformers, and the issues like uneven power sharing and circulating current between different modules can be avoided, and thus, control is simplified.

The most popular control strategy for the DAB converters is the single-phase-shift (SPS) control scheme, where the magnitude and direction of the transferred power is controlled by regulating a phase-shift angle between the two-

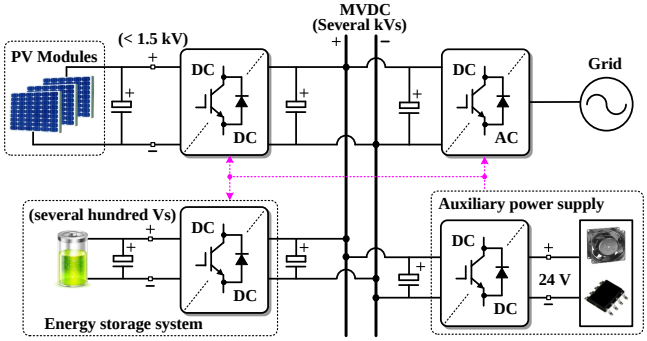

Fig. 1. A typical medium-voltage-DC (MVDC) structure to integrate large-scale PV plants and energy storage systems into the grid.

Manuscript received April 28, 2022; revised September 16, 2022 and November 24, 2022; accepted December 29, 2022. This work was supported in part by the research project Reliable Power Electronic based Power Systems (REPEPS) by the Velux Foundations under Award 00016591, and in part by the National Natural Science Foundation of China under Grant 52107212. (*corresponding author: Yongheng Yang*.)

Chaochao Song, Ariya Sangwongwanich, and Frede Blaabjerg are with the AAU Energy, Aalborg University, 9220 Aalborg, Denmark (e-mail: chso@energy.aau.dk, ars@energy.aau.dk, fbl@energy.aau.dk).

Yongheng Yang is with the College of Electrical Engineering, Zhejiang University, Hangzhou 310027, China (e-mail: yang_yh@zju.edu.cn).

Yiwei Pan is with the Digital Power Technology & Strategy Dept, Huawei Digital Power Technologies, Shanghai 201206, China (e-mail: cinsdllpyv@163.com).

TABLE I
CURRENT-RELATED OPTIMAL CONTROL STRATEGIES FOR VARIOUS DAB CONVERTERS

DAB converters	References	Optimization objectives	Control schemes	Optimization methods	Solutions	Sensors
Two-level DAB	[19]	RMS current	TPS	GOC[1] method	Analytical	2 VSs[4]
	[26]	Peak current	TPS	LMM[2] method		2 VSs
	[27]	RMS current	TPS	PSO[3] and re-arranging power model		2 VSs + 2 CSs[5]
	[28]	RMS current	EPS	Differential extremum method		2 VSs + 1 CS
	[29]	Peak current	TPS	Differential extremum method		2 VSs + 2 CSs
Multi-level DAB	[9]	RMS current	Five-level	Numerical computation algorithms	Numerical	2 VSs + 1 CS
	[30]	Peak current	Three-level	PSO method		2 VSs
	[31]	RMS current	Five-level	Numerical computation algorithms		2 VSs
	Proposed modulation	Peak current	Five-level	KKT and numerical-solution analysis	Analytical	2 VSs

1: Global optimal condition, 2: Lagrange multiplier method, 3: Particle swarm optimization, 4: voltage sensors, 5: current sensors

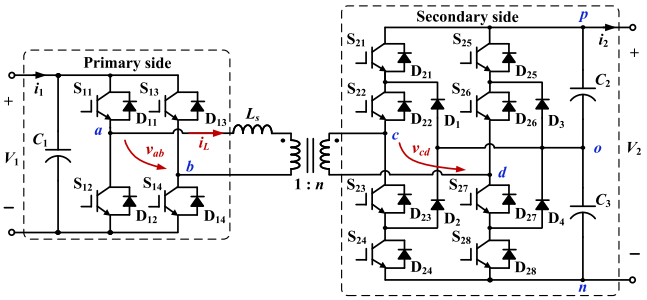

Fig. 2. A two-three (2/3)-level dual-active-bridge (DAB) DC-DC converter: V_1 and V_2 are the DC voltages, v_{ab} and v_{cd} are the terminal voltages of the isolated transformer with the turns-ratio being $1:n$, and i_L is the current of the series inductor L_s.

side bridges. The SPS control is also the simplest control strategy. However, when the two terminal voltages of the transformer are mismatched, the soft-switching operating range of the DAB converters will be limited, and the peak value and root-mean-square (RMS) of the inductor current will be significantly increased [2], [3]. Consequently, the efficiency and reliability of the DAB converters will be decreased. To overcome these issues, several multi-phase-shift (MPS) control schemes were proposed in the literature, e.g., extended-phase-shift (EPS) control, dual-phase-shift (DPS) control, triple-phase-shift (TPS) control, and five-level control [7]–[12]. In addition to these symmetric control schemes, some asymmetric modulation schemes (i.e., the waveforms of the transformer terminal voltage v_{ab} or v_{cd} is asymmetric during each switching period by modifying the duty cycle) were also proposed mainly to improve the light-load efficiency by achieving soft-switching and reducing backflow power [16]–[18]. Among them, five-level control is one of the most advantageous strategies for the NPC-based DAB converters due to more DoFs. Unfortunately, most relevant research about the five-level control only focused on the capacitor voltage balancing issue [7], [9]–[12]. The operating constraints, modeling, and optimal modulation considering the efficiency indices, e.g., current stress and reactive power, have not been fully explored.

Nevertheless, the optimal control of the 2/3-level DAB converters is achieved with three steps, i.e., operating constraints analysis, modeling, and optimal solutions calculation. Above all, operating constraints should be analyzed to ensure reliable operation of the DAB converters. Within the operating constraints, the employed switching states should decouple the voltage v_{cd} from the polarity of the inductor current i_L. Otherwise, the waveform of the voltage v_{cd} will be distorted at the zero-crossing point of the inductor current i_L. In addition, the ranges of the control variables, i.e., phase-shift angles and duty cycles, should also be limited to avoid damaged performance, e.g., higher peak current. Subsequently, the modeling of the transferred power and the optimal objectives, e.g., current stress and power loss, needs to be developed, which is essential for efficient control of the DAB converters. In most of the state-of-the-art research for the DAB converters, the modeling process is done by piecewise integration between voltage v_{ab} and current i_L, since the slopes of the current waveform differ during various intervals [19], [20]. This will, however, result in heavy computational burdens when being applied to the 2/3-level DAB converters with the five-level control scheme, due to the increased amount of intervals and operating modes. As an alternative, an equivalent-wave modeling method can be employed to simplify the modeling as discussed in [19], [21], where the transferred power model can be obtained based on the equivalent voltage waveforms without calculating the inductor current. Nevertheless, this method was proposed for the two-level DAB converters. When applying it to the 2/3-level DAB converters, the equivalent waves and calculating process should be reconsidered due to the increased voltage levels in the NPC bridge.

Then, optimal modulation solutions can be developed to improve the performance of the DAB converters. Several efficient modulation strategies have been proposed to reduce the power losses of the traditional two-level DAB converters based on the entire efficiency model or power loss model [22], [23]. However, the obtained optimal solutions from those methods are numerical since their models are dependent on various factors, e.g., conduction and switching losses of the semiconductors, copper and core losses of the transformer and auxiliary inductor. Thus, those optimal solutions should be calculated offline and pre-stored in a look-up table in micro-controllers. To reduce the control complexity, some current-related optimal control strategies, where the RMS current and peak current were applied as the optimization objectives, have been proposed since the current-related models are simpler than the power loss or efficiency models [19], [24]–[31], as

shown in Table I. It can be seen from Table I that analytical solutions were generally applied to two-level DAB converter while numerical solutions were applied to the multi-level DAB converters. That is because with the increased number of control variables (i.e., DoFs), the optimization methods used in two-level DAB converter are challenging to be applied to the multi-level DAB converters. For instance, the expressions of two phase-shift angles were obtained based on the numerical solutions in the TPS control for the two-level DAB converter in [27], and the last phase-shift angle can be directly obtained by substituting the two phase-shift angles into the power model. However, this method cannot be extended to the NPC-based DAB converters with five-level control due to the increased number of control variables. The control strategies with numerical solutions have some limitations in practice as: (1) the control strategies with numerical solutions require pre-calculation of the optimal control variables offline and look-up tables in the microcontroller. When the parameters (e.g., input and output voltages) change, the optimal control variables should be re-calculated, which results in heavy calculation burdens; (2) the continuity of the control variables along with the transferred power may not be achieved when using numerical solutions, which will affect the dynamics (e.g., large output voltage and current fluctuation) of the converter when the transferred power changes in a closed-loop control system.

In light of the above, the three steps for optimal control are comprehensively analyzed in this paper. Firstly, the operating constraints for the 2/3-level DAB converters are derived based on the switching characteristics analysis in Section II. With the constraints, the power model and current stress model under different operating modes are obtained in Section III by using the equivalent-wave method to reduce the computational burdens and simplify the modeling process. Subsequently, in Section IV, a minimum-current-stress (MCS) modulation scheme is proposed, in which the optimal analytical solutions for the control variables are derived by combining the Karush-Kuhn-Tucker (KKT) conditions and the numerical-solution analysis. Furthermore, a closed-loop control system is designed to modify the control variables along with the reference transferred power/output voltage. In the closed-loop control system, the input and output current sensors can be avoided. Therefore, the hardware cost and the control complexity for the 2/3-level DAB converters can be reduced. Experimental results are given in Section V to verify the effectiveness of the theoretical analysis. Finally, a conclusion is provided in Section VI. The novelty of this paper can be summarized as:

- Operating constraints for the NPC-based DAB converters are first discussed, which are applied to the control strategies to avoid voltage and current distortions and overshoots.
- An optimization method by combining the numerical-solution analysis with the KKT conditions is proposed to obtain the analytical solutions. In this method, the numerical solutions are applied to determine certain operating modes where the optimal solutions are located and simplify the constraints in the KKT conditions. By doing so, the analytical solutions can be easily obtained.

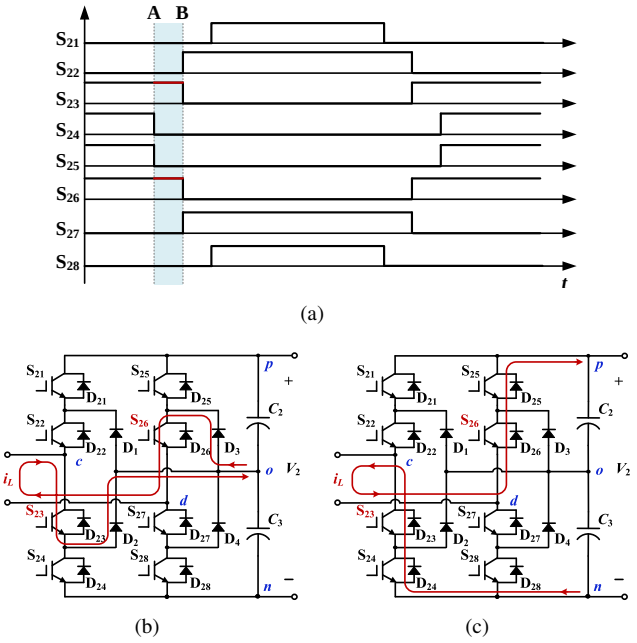

Fig. 3. A typical modulation scheme where the waveforms are dependent of the current polarity. (a) Switching sequence for the NPC bridge. (b) Current conduction path when i_L is positive during [A, B]. (c) Current conduction path when i_L is negative during [A, B].

- A generic optimal control strategy is proposed to minimize the current stress and to improve the efficiency, where the control variables can be automatically regulated online and the optimum operation can be ensured even when the operating parameters vary in a wide range. This cannot be achieved in the previous control strategies for the multi-level DAB converters based on the numerical solutions [9], [30], [31], where the control parameters should be pre-calculated.

This paper is extended from [32], where the operating constraints and power modeling were analyzed for the 2/3-level DAB converters. Compared to [32], the proposed MCS modulation scheme, and the experimental verification for the operating constraints and the MCS modulation are presented in this paper.

II. Operating Constraints for 2/3-level DAB

A. Universal Operating Constraint for NPC-Based DAB

For the 2/3-level DAB converters, the terminal voltage v_{cd} of the NPC bridge can be two-level ($v_{cd} \in \{\pm V_2\}$) [33], three-level ($v_{cd} \in \{0, \pm V_2\}$) [8], four-level ($v_{cd} \in \{\pm 0.5V_2, \pm V_2\}$) [34], and five-level ($v_{cd} \in \{0, \pm 0.5V_2, \pm V_2\}$) [9], [10] depending on the applied modulation strategies. Regardless of the modulation strategies, the voltage v_{cd} should not be affected by the polarity of the inductor current i_L. Otherwise, the waveforms of v_{cd} and i_L will be distorted. For instance, a modulation strategy with the switching sequence shown in Fig. 3 (a) was proposed for capacitor voltage balancing [7]. It can be seen that during the interval [A, B], the ON switches are $\{S_{23}, S_{26}\}$. If the inductor current i_L during this interval is positive (from the primary side to secondary side), the current

TABLE II
SWITCHING STATES FOR NPC BRIDGE

Switching state	ON switches (first arm)	ON switches (second arm)	v_{cn}/v_{dn}
[P]	$\{S_{21}, S_{22}\}$	$\{S_{25}, S_{26}\}$	V_2
[O]	$\{S_{22}, S_{23}\}$	$\{S_{26}, S_{27}\}$	$0.5V_2$
[N]	$\{S_{23}, S_{24}\}$	$\{S_{27}, S_{28}\}$	0

will flow through D_3, S_{26}, S_{23} and D_2, as shown in Fig. 3 (b). Thus, the voltage v_{cd} during this interval is 0. On the other hand, if the inductor current during this interval is negative, the current will flow through D_{24}, D_{23}, D_{26} and D_{25}, as shown in Fig. 3 (c), and the voltage v_{cd} is $-V_2$. Therefore, although the switching sequence keeps constant, the voltage v_{cd} will change with different inductor current polarity. The polarity of the inductor current is difficult to be determined online, because it is affected by the phase-shift angles, duty cycles of the gate-driving signals, two-side DC voltages, and so on. Thus, the voltage distortion can easily occur when applying the modulation scheme in [7], especially when the zero-crossing point of the inductor current i_L changes during the interval [A, B]. In addition, the inductor current will be further affected by the change in the voltage v_{cd} according to the expression of i_L, i.e.,

$$\frac{di_L(t)}{dt} = \frac{v_{ab}(t) - v_{cd}(t)/n}{L_s} \tag{1}$$

Moreover,the transferred power of DAB converters is expressed as

$$P = \frac{1}{T_{hs}} \int_0^{T_{hs}} v_{ab}(t) i_L(t) dt \tag{2}$$

which will also be affected by the polarity of the inductor current, and thus, it will significantly increase the complexity of power modeling and reduce the reliability of the modulation scheme.

To avoid the above issues, the employed switching states should ensure that the voltage v_{cd} is independent of the inductor current polarity. Therefore, the possible switching states which satisfy the above description are summarized in Table II, where v_{cn}/v_{dn} denotes the voltage between the midpoint c/d of each arm and the negative pole n in Fig. 2. Thus, the switching sequence should be the combinations of the switching states in the first and second arms shown in Table II (e.g., [PP]), i.e., the ON switches should be $\{S_{2i}, S_{2(i+1)}\}$, (i = 1, 2, 3 for the first arm, and i = 5, 6, 7 for the second arm) during any interval. This principle is defined as the universal operating constraint for the NPC-based DAB converters with all phase-shift control strategies.

B. Operating Constraints for the Five-Level Control

Based on the above analysis, a five-level control scheme shown in Fig. 4 is employed for the 2/3-level DAB converters, in which T_{hs} is half of a switching cycle, $v'_{cd} = v_{cd}/n$ denotes the secondary-side voltage v_{cd} after being converted to the primary side. The transferred power of the converters is controlled by the four control variables D_0, D_1, D_2, and D, where D_0, D_1, and D_2 are the phase-shift ratios between

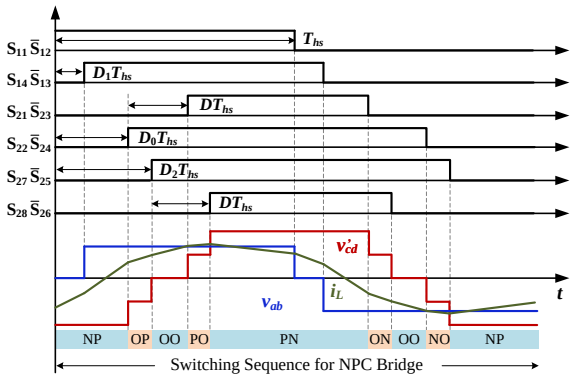

Fig. 4. Waveforms for 2/3-level DAB converters with the five-level control.

S_{14} and S_{11}, S_{27} and S_{11}, and S_{22} and S_{11}, respectively, and D is the duty-cycle ratio of the gate-driving signals for the secondary-side switches. The ranges of the four control variables are defined between 0 and 1. It should be noted that whether D_2 is larger or less than D_0, the waveforms of v_{ab}, v_{cd}, and i_L remain unchanged, which means the performances of the converters will be the same with different relationships between D_2 and D_0. A similar condition applies also for the relationship between D_2 and $D_0 + D$. Therefore, to simplify the modeling, only the condition $D_0 \le D_2 \le D_0 + D$ is considered.

Moreover, as shown in Fig. 4, $D_2 + D$ is the largest phase-shift ratio, whose maximum value should be further discussed. Fig. 5 shows the waveforms under the condition $D_2 + D > 1 + D_0$, from which, it can be seen that the highest voltage levels $\pm V_2$ will not appear. That is because the switching state which can achieve the positive highest voltage level, i.e., $v_{cd} = V_2$, is [PN], and which can achieve the negative highest voltage level, i.e., $v_{cd} = -V_2$, is [NP]. However, if $D_2 + D > 1 + D_0$, the two switching states [PN] and [NP] will not be utilized. As a result, the voltage waveform with the five-level control scheme will in fact be limited to three levels, and the power transmission capability will also be reduced. Based on the above analysis, the operating constraints for the five-level control scheme can be summarized as

$$\begin{cases} 0 \le D_1 \le 1 \\ 0 \le D_0 \le D_2 \le (D_0 + D) \le (D_2 + D) \le (1 + D_0) \end{cases} \tag{3}$$

III. MODELING OF 2/3-LEVEL DAB CONVERTERS

A. Unified Transferred Power Model

From Fig. 4, it can be seen that the voltages v_{ab} and v_{cd} are three-level and five-level symmetric square waves, respectively. Therefore, the waveform of the inductor current i_L is divided into various intervals with different slopes according to (1). In the traditional modeling, to calculate the transferred power, the current slopes and values during different intervals should be calculated separately, and then integrated piece by piece according to (2). Thus, the traditional method will lead to a heavy computational burden when being applied to 2/3-level DAB converters.

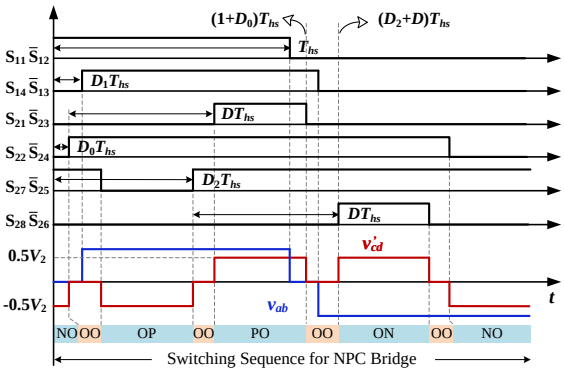

Fig. 5. Waveforms for 2/3-level DAB converters when $D_2 + D > 1 + D_0$.

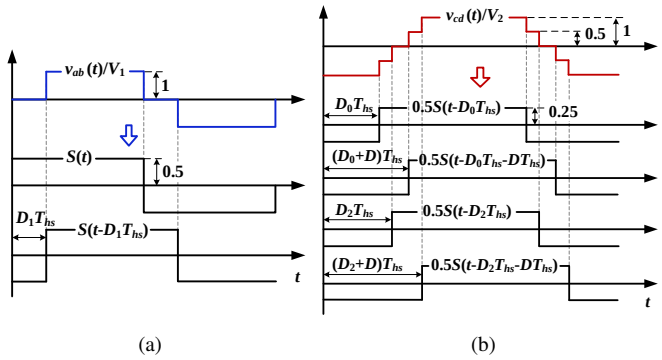

(a) (b)

Fig. 6. Equivalent waves for the terminal voltages v_{ab} and v_{cd}. (a) Equivalent waves for v_{ab}. (b) Equivalent waves for v_{cd}.

In the equivalent-wave modeling method, the waveforms of v_{ab} and v_{cd} can be decomposed into two and four square waves with 50% duty cycle, respectively, as shown in Fig. 6. $S(t)$ denotes the basic wave whose period is equal to the switching period $2T_{hs}$, and the amplitude is 0.5. The other waves are obtained by phase shifting $S(t)$, and denoted as $S(t - xT_{hs})$, where x is the phase-shift ratios. For the primary-side voltage v_{ab}, the phase-shift ratios are 0 and D_1, and thus, it can be equivalent to two square waves $S(t)$ and $S(t - D_1T_{hs})$. On the other hand, four different phase-shift ratios appear in the secondary-side voltage v_{cd}, i.e., D_0, D_2, $D_0 + D$, and $D_2 + D$. Therefore, the waveform of v_{cd} can be decomposed into four equivalent waves: $S(t - D_0T_{hs})$, $S(t - D_2T_{hs})$, $S(t - D_0T_{hs} - DT_{hs})$, and $S(t - D_2T_{hs} - DT_{hs})$. In this way, the equivalent circuit of the 2/3-level DAB converter can be depicted as shown in Fig. 7.

According to (1) and Fig. 7, the inductor current i_L can be expressed as

$$i_L(t) = \frac{1}{L_s}\left\{V_1 \sum_{i=1}^{2} T_r(t - x_iT_{hs}) - \frac{V_2}{2n}\sum_{j=1}^{4} T_r(t - x_jT_{hs})\right\} \tag{4}$$

where $x_i \in \{0, D_1\}$ $(i = 1, 2)$ denotes the phase-shift ratios in the primary side, and $x_j \in \{D_0, D_2, D_0 + D, D_2 + D\}$ $(j = 1, 2, 3, 4)$ denotes the phase-shift ratios in the secondary side. $T_r(t)$ is the integration of $S(t)$, whose expression during

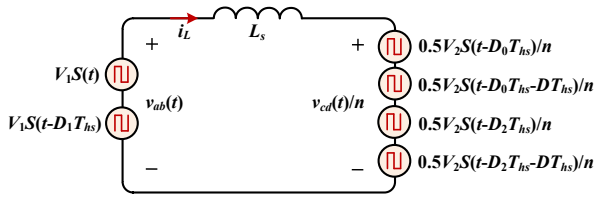

Fig. 7. Equivalent circuit of the 2/3-level DAB converter by using the equivalent-wave method.

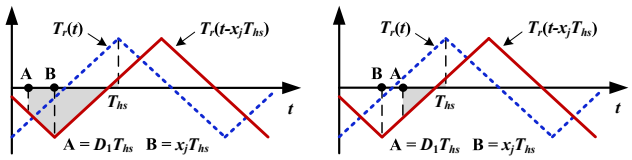

(a) (b)

Fig. 8. Two conditions for calculating the transferred power: (a) $D_1 \le x_j$, and (b) $D_1 > x_j$.

one switching cycle can be given as

$$T_r(t) = \begin{cases} 0.5t - 0.25T_{hs}, & 0 \le t < T_{hs} \\ -0.5t + 0.75T_{hs}, & T_{hs} \le t < 2T_{hs} \end{cases} \tag{5}$$

Combining (2) and (4), the unified expression of the transferred power can be obtained as

$$P = \frac{-V_1V_2}{2nL_rT_{hs}} \sum_{j=1}^{4} \int_{D_1T_{hs}}^{T_{hs}} T_r(t - x_jT_{hs})dt \tag{6}$$

B. Transferred Power and Current Stress Expressions During Each Operating Mode

From (6), it can be seen that two conditions should be discussed when calculating

$$\int_{D_1T_{hs}}^{T_{hs}} T_r(t - x_jT_{hs})dt \tag{7}$$

i.e., $D_1 \le x_j$ and $D_1 > x_j$, as shown in Fig. 8. Under the condition $D_1 \le x_j$, two intervals $[D_1T_{hs}, x_jT_{hs}]$ and $[x_jT_{hs}, T_{hs}]$ should be considered due to the piecewise expression of $T_r(t - x_j)$, as shown in Fig. 8 (a). On the other hand, under the condition $D_1 > x_j$, only one interval $[D_1T_{hs}, T_{hs}]$ should be considered, as shown in Fig. 8 (b). Based on (5), the integration of the two conditions can be calculated as

$$\int_{D_1T_{hs}}^{T_{hs}} T_r(t - x_jT_{hs})dt = \begin{cases} 0.25(2x_j^2 + D_1^2 - 2x_jD_1 - 2x_j + D_1)T_{hs}^2, & D_1 \le x_j \\ 0.25(-D_1^2 + 2x_jD_1 - 2x_j + D_1)T_{hs}^2, & D_1 > x_j \end{cases} \tag{8}$$

Therefore, with different relationships between D_1 and the four phase-shift ratios x_j $(j = 1, 2, 3, 4)$ in the secondary side, the power expressions will change, and the DAB converter operates at different modes. According to the operating constraints of the control variables (i.e., Eq. (3)), the relationships among the four phase-shift ratios in the secondary side is

TABLE III
NORMALIZED PEAK CURRENT MODEL FOR 2/3-LEVEL DAB CONVERTERS WITH THE FIVE-LEVEL CONTROL

Modes	Normalized peak current model i_0		
	$0 < k \leq 0.5$	$0.5 < k \leq 1$	$k > 1$
Mode 1	$2\left[-kD_1 + 2kD_0 + (2k-1)D - k + 1\right]$	$2\left[-kD_1 + (2k-1)D_2 + D_0 + (2k-1)D - k + 1\right]$	$2\left[-kD_1 + D_2 + D_0 + D + k - 1\right]$
Mode 2			
Mode 3			
Mode 4	$2\left[kD_1 - D - k + 1\right]$	$2\left[kD_1 - D - k + 1\right]$	$2\left[-kD_1 + D_2 + D_0 + D + k - 1\right]$
Mode 5			

determined as $D_0 \leq D_2 \leq (D_0+D) \leq (D_2+D)$. Therefore, under different relationships between D_1 and x_j, five operating modes can be divided as

$$\begin{cases} D_1 \leq D_0 \leq D_2 \leq (D_0+D) \leq (D_2+D), & \text{Mode 1} \\ D_0 < D_1 \leq D_2 \leq (D_0+D) \leq (D_2+D), & \text{Mode 2} \\ D_0 \leq D_2 < D_1 \leq (D_0+D) \leq (D_2+D), & \text{Mode 3} \\ D_0 \leq D_2 \leq (D_0+D) < D_1 \leq (D_2+D), & \text{Mode 4} \\ D_0 \leq D_2 \leq (D_0+D) \leq (D_2+D) < D_1, & \text{Mode 5} \end{cases} \quad (9)$$

The voltages and current waveforms under the five operating modes are shown in Fig. 9. Note that these five modes are obtained under the constraint that all of the phase-shift ratios are no larger than 1. Without this constraint, there will be more modes, e.g., Mode 6 and Mode 7 in Fig. 10. However, these modes will not broaden the power-transfer range, and the performance of the DAB converter will be decreased, e.g., the peak current will be increased. Therefore, Modes 1 to 5 are discussed for minimizing the current stress. Subsequently, the transferred power of each mode can be calculated according to (6) and (8). For instance, $D_1 \leq x_j$ $(j = 1, 2, 3, 4)$ for Mode 1, the transferred power is obtained as

$$\begin{aligned} P &= \frac{-V_1 V_2}{2nL_r T_{hs}} \sum_{j=1}^{4} 0.25(2x_j^2 + D_1^2 - 2x_j D_1 - 2x_j + D_1) T_{hs}^2 \\ &= \frac{V_1 V_2 T_{hs}}{2nL_r}(-D_1^2 - D_2^2 - D_0^2 - D^2 + D_1 D_2 + D_1 D_0 \\ &\quad + D_1 D - D_2 D - D_0 D - D_1 + D_2 + D_0 + D) \end{aligned} \quad (10)$$

In a similar way, the transferred power for other modes can be obtained as shown in (11). The normalized power is defined as $P_0 = P/P_N$, where $P_N = V_1 V_2 T_{hs}/(4nL_s)$ is the maximum transferred power of the DAB converters. In this way, the relationship between D_1 and x_j is the only factor to be considered for calculating the power expressions in different operating modes instead of the current slopes and values during various intervals as in the traditional modeling method.

Furthermore, the peak value of the inductor current i_L for the 2/3-level DAB converters can be calculated according to (4) and (5). It can be seen from (1) that the peak current will appear at different time in a switching cycle under various relationships between v_{ab} and v'_{cd} (i.e., v_{cd}/n). For instance, the peak current for Mode 1 appears at: 1) $t = (D_0+D)T_{hs}$ when $0 < k \leq 0.5$, 2) $t = (D_2+D)T_{hs}$ when $0.5 < k \leq 1$, and 3) $t = T_{hs}$ when $k > 1$, where k is the voltage conversion ratio, which is defined as $k = nV_1/V_2$. The normalized peak current of each mode under different ranges of the voltage conversion ratio k is shown in Table III. Note that the normalized peak current is defined as $i_0 = i_p/I_N$, where i_p is the peak current, and $I_N = V_2 T_{hs}/(4nL_s)$.

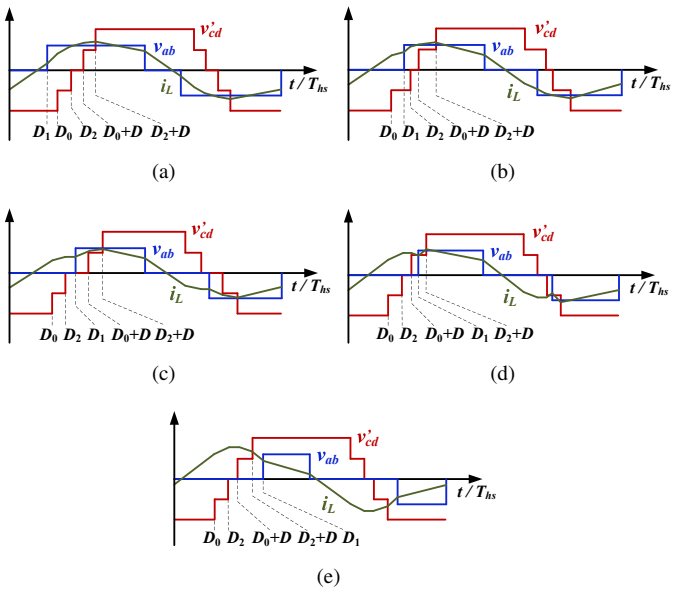

Fig. 9. Waveforms of the 2/3-level DAB converters under: (a) Mode 1, (b) Mode 2, (c) Mode 3, (d) Mode 4, and (e) Mode 5.

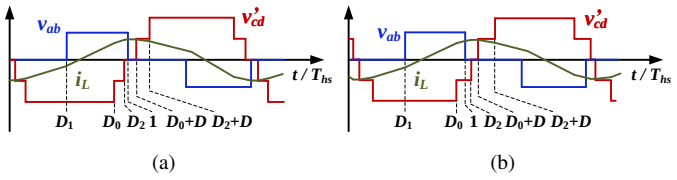

Fig. 10. Waveforms of the 2/3-level DAB converters under: (a) Mode 6: $D_1 \leq D_0 \leq D_2 \leq 1 \leq (D_0+D) \leq (D_2+D)$, and (b) Mode 7: $D_1 \leq D_0 \leq 1 \leq D_2 \leq (D_0+D) \leq (D_2+D)$.

IV. PROPOSED OPTIMAL MODULATION TO MINIMIZE THE CURRENT STRESS

From the transferred power model in (11), it can be seen that to achieve a certain reference transferred power, different combinations of the control variables D_1, D_2, D_0, and D can be employed. However, with these variables, the current stress will be different (see Table III). Therefore, it is necessary to

$$P_0 = \begin{cases} 2(-D_1^2 - D_2^2 - D_0^2 - D^2 + D_1D_2 + D_1D_0 + D_1D - D_2D - D_0D - D_1 + D_2 + D_0 + D), & \text{Mode 1} \\ 2(-0.5D_1^2 - D_2^2 - 0.5D_0^2 - D^2 + D_1D_2 + D_1D - D_2D - D_0D - D_1 + D_2 + D_0 + D), & \text{Mode 2} \\ 2(-0.5D_2^2 - 0.5D_0^2 - D^2 + D_1D - D_0D - D_2D - D_1 + D_2 + D_0 + D), & \text{Mode 3} \\ 2(0.5D_1^2 - 0.5D_2^2 - 0.5D^2 - D_1D_0 - D_2D - D_1 + D_2 + D_0 + D), & \text{Mode 4} \\ 2(D_1^2 - D_1D_2 - D_1D_0 - D_1D - D_1 + D_2 + D_0 + D), & \text{Mode 5} \end{cases} \tag{11}$$

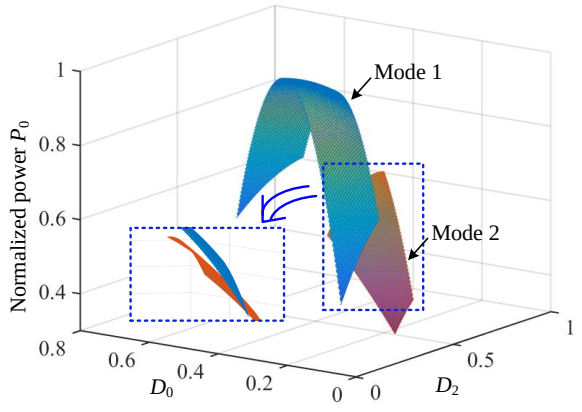

Fig. 11. Normalized transferred power range for Mode 1 (D_1 = 0.1, D = 0.2) and Mode 2 (D_1 = 0.2, D = 0.3).

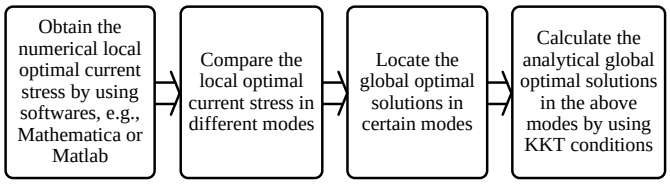

Fig. 12. Calculating process for the analytical optimal solutions.

discuss the optimal combinations of the control variables to minimize the current stress during the entire power range.

A. Optimal Solutions for Minimizing the Current Stress

The optimization problem for minimizing the current stress can be described as

$$\begin{aligned} &\min \quad i_0(\boldsymbol{X}) \\ &s.t. \quad P_0(\boldsymbol{X}) - P_0^* = 0 \\ &\quad\; f_i(\boldsymbol{X}) \le 0, i = 1, 2, \cdots m \end{aligned} \tag{12}$$

where $\boldsymbol{X} = (D_1, D_2, D_0, D)$ indicates the set of the control variables, P_0^* is the reference transferred power, and $f_i(\boldsymbol{X})$ is the set of the operating constraints. Analytical solutions and numerical solutions are two types of solutions for such an optimization problem. The numerical solutions are generally employed in the applications where the reference transferred power/output voltage varies in a narrow range. Otherwise, a heavy computational burden and extra memory of the microcontroller for pre-storing the numerical solutions will be required. On the other hand, the analytical solutions, which are expressed by the transferred power P_0 and the voltage conversion ratio k, can realize the online optimal control automatically when the operating conditions change. Therefore, the analytical solutions are more suitable in practice.

The KKT conditions are popular for acquiring the analytical solutions for the optimization problems, which can be described as

$$\begin{cases} E(\boldsymbol{X}, \lambda, \mu_i) = i_0(\boldsymbol{X}) + \lambda(P_0(\boldsymbol{X}) - P_0^*) + \sum_{i=1}^{m} \mu_i f_i(\boldsymbol{X}) \\ \dfrac{\partial E}{\partial \boldsymbol{X}}\Big|_{\boldsymbol{X}=\boldsymbol{X}^*} = 0, \mu_i f_i(\boldsymbol{X}^*) = 0, f_i(\boldsymbol{X}^*) \le 0, \lambda \ne 0, \mu_i \ge 0 \end{cases} \tag{13}$$

where $E(\boldsymbol{X}, \lambda, \mu_i)$ denotes the Lagrangian, $\boldsymbol{X}^* = (D_1^*, D_2^*, D_0^*, D^*)$ denotes the optimal solutions, λ and μ_i are the KKT multipliers.

The transferred power ranges during different operating modes may coincide, i.e., for a certain transferred power, different combinations of the control variables can be applied, and the DAB converters will operate under different modes according to (9). For instance, Fig. 11 shows the ranges of the normalized transferred power P_0 for Mode 1 and Mode 2, where the control variables D_1 = 0.1, D = 0.2 is applied in Mode 1, and D_1 = 0.2, D = 0.3 is applied in Mode 2. It can be seen from Fig. 11 that various control variables in the two modes can realize identical transferred power in certain ranges. Thus, there will be two steps to obtain the optimal solutions for minimizing the current stress: 1) the optimal solutions $(D_1^*, D_2^*, D_0^*, D^*)$ and the corresponding peak current during each operating mode should be obtained, which are defined as local optimal solutions and local minimum peak current; 2) the local minimum peak current should be compared among different operating modes to obtain the global optimal solutions. Furthermore, obtaining the analytical solutions by directly utilizing the KKT conditions will be challenging, due to four control variables and various operating constraints ((3) and (9)). To simplify the calculating process, at first, the numerical solutions are employed to compare the local optimal solutions in each operating mode. In this way, the global optimal solutions in different power ranges can be located in certain operating modes. In all, the steps for obtaining the analytical optimal solutions is summarized in Fig. 12. The calculating process for the condition $0 < k \le 0.5$ will be detailed, while that of the other conditions $0.5 < k \le 1$ and $k > 1$ can be analyzed similarly.

Fig. 13 depicts the curves of the local minimum current stress in each mode, which are calculated by Mathematica. As shown in Fig. 13, two power boundaries P_A and P_B divide the entire transferred power into three ranges. When $P_B < P_0 \le 1$, the local minimum current stress of Mode 1 is lower than that of any other mode, which means the global

optimal solutions during this power range are located in Mode 1. Similarly, when $P_A < P_0 \leq P_B$ and $0 < P_0 \leq P_A$, the global optimal solutions are located in Mode 2 and Mode 3, respectively. Furthermore, the local optimal numerical solutions corresponding to the minimum current stress in Mode 1, 2, and 3 under the three power ranges are shown in Fig. 14, which is also the global optimal solutions during the entire range. The process to obtain the analytical solutions can be further simplified according to the characteristics of the numerical solutions. For instance, it can be seen from Fig. 14 that with different voltage conversion ratio k, D_1^* = 0 can be satisfied during $P_B < P_0 \leq 1$. Therefore, when calculating the analytical solutions of Mode 1 by using KKT conditions, $D_1^* = 0$ can be substituted to (13). Similarly, $D_0^* = 0$ holds when calculating the analytical solutions of Mode 2 and Mode 3 during $P_A < P_0 \leq P_B$ and $0 < P_0 \leq P_A$, respectively. It should be noted that the numerical solutions are only utilized to locate the optimal solutions and simplify the calculating process. Ultimately, the 2/3-level DAB converters will operate with the analytical solutions.

With the above analysis, the KKT conditions for Mode 1 are expressed as

$$\begin{cases} E = 2\left[2kD_0 + (2k-1)D - k + 1\right] + \lambda[2(-D_0^2 - D_2^2 \\ \quad -D^2 - D_2D - D_0D + D_2 + D_0 + D) - P_0^*)] \\ \quad +\mu_1(D_0 - D_2) + \mu_2(D_2 - D_0 - D) \\ \quad +\mu_3(D_2 + D - 1) + \mu_4(-D_0) \\ \dfrac{\partial E}{\partial D_2} = 0, \dfrac{\partial E}{\partial D_0} = 0, \dfrac{\partial E}{\partial D} = 0 \\ \lambda \neq 0, \mu_i \geq 0, i = 1,2,3,4 \\ \mu_1(D_0 - D_2) = 0, \mu_2(D_2 - D_0 - D) = 0, \\ \mu_3(D_2 + D - 1) = 0, \mu_4(-D_0) = 0, D_0 - D_2 \leq 0, \\ D_2 - D_0 - D \leq 0, D_2 + D - 1 \leq 0, -D_0 \leq 0 \end{cases} \tag{14}$$

Furthermore, from the numerical solutions shown in Fig. 14, it can be seen that the constraints $f_i(\boldsymbol{X}^*) < 0$ (i.e., $D_0 - D_2 < 0$, $D_2 - D_0 - D < 0$, $D_2 + D - 1 < 0$, and $-D_0 < 0$) are satisfied during $P_B < P \leq 1$. Due to $\mu_i f_i(\boldsymbol{X}^*) = 0$, it can be derived that $\mu_i = 0$ $(i = 1,2,3,4)$. Thus, (14) can be simplified as

$$\begin{cases} \dfrac{\partial E}{\partial D_2} = 2\lambda(-2D_2 - D + 1) = 0, \\ \dfrac{\partial E}{\partial D_0} = 4k + 2\lambda(-2D_0 - D + 1) = 0, \\ \dfrac{\partial E}{\partial D} = 2(2k-1) + 2\lambda(-D_2 - D_0 - 2D + 1) = 0, \end{cases} \tag{15}$$

from which, the relationships among the optimal control variables can be obtained as

$$D_1^* = 0, D_2^* = \frac{1 - D^*}{2}, D_0^* = \frac{1}{2} + \frac{k+1}{2(k-1)}D^* \tag{16}$$

Combining (16) with the power of Mode 1 in (11), the optimal

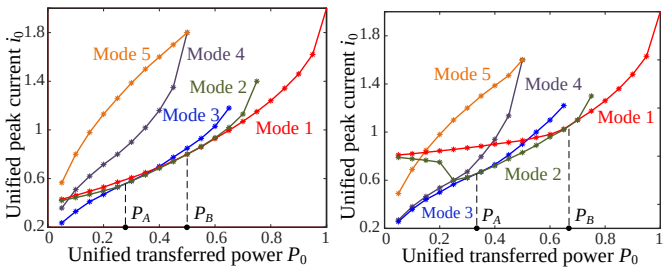

Fig. 13. Curves of the local minimum current stress in each mode with different voltage conversion ratios. (a) $k = 0.2$. (b) $k = 0.4$.

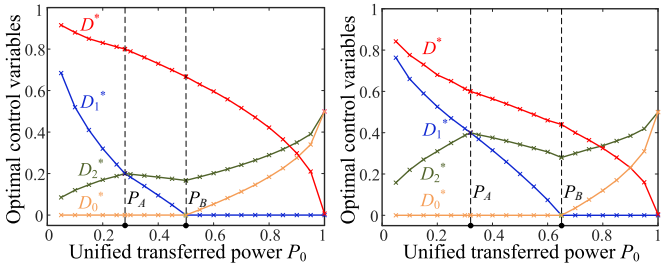

Fig. 14. Curves of the global optimal numerical solutions with different voltage conversion ratios. (a) $k = 0.2$. (b) $k = 0.4$.

analytical solutions of Mode 1 can be obtained as

$$\text{Mode 1}: \begin{cases} D_1^* = 0, \\ D_2^* = \dfrac{1}{2} - \dfrac{1-k}{2}\sqrt{\dfrac{1-P_0}{3k^2-2k+1}}, \\ D_0^* = \dfrac{1}{2} - \dfrac{1+k}{2}\sqrt{\dfrac{1-P_0}{3k^2-2k+1}}, \\ D^* = (1-k)\sqrt{\dfrac{1-P_0}{3k^2-2k+1}} \end{cases} \tag{17}$$

In addition, the obtained analytical solutions should satisfy the operating constraints of Mode 1, i.e., $0 \leq D_1 \leq D_0 \leq D_2 \leq (D_0 + D) \leq (D_2 + D) \leq 1$. Accordingly, the power range for the optimal analytical solutions in Mode 1 can be calculated as

$$\frac{2k(2-k)}{(k+1)^2} \leq P_0 \leq 1 \tag{18}$$

In a similar way, the relationships among the optimal control variables in Mode 2 can be calculated as

$$D_1^* = \frac{1+k}{1-k}D^* - 1, D_2^* = \frac{k}{1-k}D^*, D_0^* = 0 \tag{19}$$

Combining (19) with the power expression (i.e.,(11)) and the operating constraints (i.e.,(9)) of Mode 2, the optimal solutions

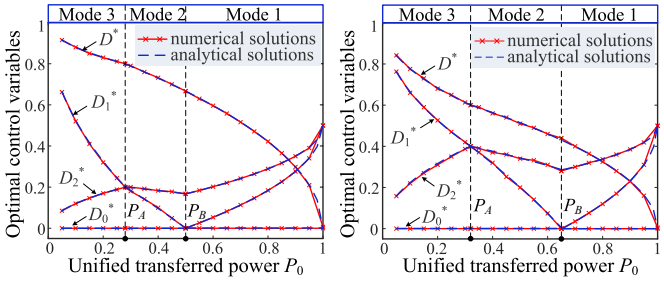

Fig. 15. Comparative curves between the numerical solutions and the analytical solutions with different voltage conversion ratios. (a) $k = 0.2$. (b) $k = 0.4$.

and power range can be obtained as

$$\text{Mode 2}: \begin{cases} D_1^* = (1+k)\sqrt{\dfrac{1-P_0}{3k^2-2k+1}} - 1, \\ D_2^* = k\sqrt{\dfrac{1-P_0}{3k^2-2k+1}}, D_0^* = 0, \\ D^* = (1-k)\sqrt{\dfrac{1-P_0}{3k^2-2k+1}}, \\ k(2-3k) < P_0 \le \dfrac{2k(2-k)}{(k+1)^2} \end{cases} \tag{20}$$

Furthermore, for Mode 3, the relationships among the optimal control variables are obtained as

$$D_1^* = \frac{2k-1+(1-k)D^*}{k}, D_2^* = 1-D^*, D_0^* = 0 \tag{21}$$

Similarly, the optimal solutions and the corresponding power range can be obtained as

$$\text{Mode 3}: \begin{cases} D_1^* = 1-(1-k)\sqrt{\dfrac{P_0}{(2-3k)k}}, \\ D_2^* = \sqrt{\dfrac{kP_0}{2-3k}}, D_0^* = 0, \\ D^* = 1-\sqrt{\dfrac{kP_0}{2-3k}}, \\ 0 < P_0 \le k(2-3k) \end{cases} \tag{22}$$

From the power ranges in (18), (20), and (22), it can be seen that the optimal solutions of the three modes can cover the entire power range (i.e., $0 < P_0 \le 1$), and the power ranges between different modes are seamless. Therefore, the two power boundaries in Fig. 14 can be obtained as

$$P_A = k(2-3k), P_B = \frac{2k(2-k)}{(k+1)^2} \tag{23}$$

To verify the effectiveness of the optimal analytical solutions, the comparative curves between the numerical solutions and the analytical solutions are illustrated in Fig. 15. It can be seen that the curves of the analytical solutions and the numerical solutions are well aligned, which means the obtained analytical solutions are global optimal solutions for minimizing the current stress. In addition, Fig. 16 shows the comparative curves of the power boundaries P_A and P_B

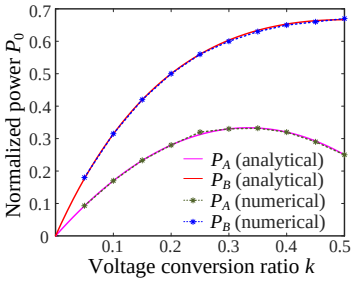

Fig. 16. Comparative curves of the power boundaries P_A and P_B between the numerical solutions and analytical solutions.

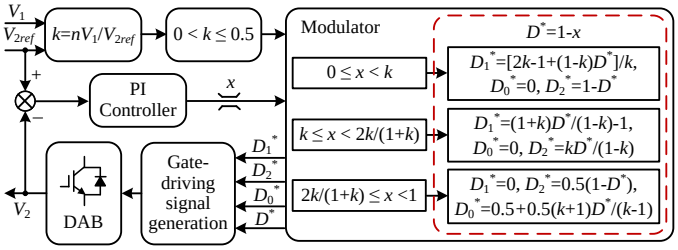

Fig. 17. Closed-loop control system for minimizing the current stress during $0 < k \le 0.5$.

between the numerical and analytical solutions, where it can be seen that the two curves are also well aligned, and the expressions of P_A and P_B in (23) are the boundaries which divide the three operating modes under different power ranges. Furthermore, it can be seen from Fig. 15 that at the two power boundaries P_A and P_B, the control variables can transfer from one operating mode to another seamlessly, which means the converters can transfer between different power ranges smoothly by using the proposed analytical solutions.

The optimal analytical solutions during $0.5 < k \le 1$ and $k > 1$ can be obtained with the similar analysis, which are summarized in Table IV. Note that although the optimal modulation is proposed based on the five-level control scheme, in some conditions, the voltage levels of the voltage v_{cd} will be less than five. For example, it can be seen from Table IV that during $k > 1$ and $2(k-1)/k^2 < P_0 \le 1$, the duty-cycle ratio D is 0, and the phase-shift ratio D_2 is equal to D_0. In such a condition, the voltage v_{cd} is a two-level square waveform, which is similar to that in the SPS and EPS control strategies.

B. Closed-Loop Control

With the obtained analytical solutions as shown in Table IV, the optimal combination of the control variables to minimize the current stress can be determined under any transferred power. However, if the transferred power P_0 is directly utilized to calculate the control variables, the online regulation of the control variables along with the operating conditions is still difficult to be achieved, due to the nonlinearity of the analytical solutions. Therefore, the closed-loop control system should be further simplified.

Fig. 17 shows the simplified closed-loop control structure for the minimum-current-stress (MCS) control scheme during $0 < k \le 0.5$, in which V_{2ref} denotes the reference output

TABLE IV
OPTIMAL SOLUTIONS FOR THE MINIMUM-CURRENT-STRESS (MCS) CONTROL SCHEME WITH DIFFERENT VOLTAGE CONVERSION RATIOS

Ranges of k	Optimal control variables				Transferred power ranges
	D_1^*	D_2^*	D_0^*	D^*	
$0 < k \leq 0.5$	$1-(1-k)\sqrt{\frac{P_0}{(2-3k)k}}$	$\sqrt{\frac{kP_0}{2-3k}}$	0	$1-\sqrt{\frac{kP_0}{2-3k}}$	$0 < P_0 \leq k(2-3k)$
	$(1+k)\sqrt{\frac{1-P_0}{3k^2-2k+1}}-1$	$k\sqrt{\frac{1-P_0}{3k^2-2k+1}}$	0	$(1-k)\sqrt{\frac{1-P_0}{3k^2-2k+1}}$	$k(2-3k) < P_0 \leq \frac{2k(2-k)}{(k+1)^2}$
	0	$\frac{1}{2}-\frac{1-k}{2}\sqrt{\frac{1-P_0}{3k^2-2k+1}}$	$\frac{1}{2}-\frac{1+k}{2}\sqrt{\frac{1-P_0}{3k^2-2k+1}}$	$(1-k)\sqrt{\frac{1-P_0}{3k^2-2k+1}}$	$\frac{2k(2-k)}{(k+1)^2} < P_0 \leq 1$
$0.5 < k \leq 1$	$1-k\sqrt{\frac{P_0}{(1-k)(3k-1)}}$	$\sqrt{\frac{(1-k)P_0}{3k-1}}$	0	$1-k\sqrt{\frac{P_0}{(1-k)(3k-1)}}$	$0 < P_0 \leq (1-k)(3k-1)$
	$(2-k)\sqrt{\frac{1-P_0}{3k^2-4k+2}}-1$	$(1-k)\sqrt{\frac{1-P_0}{3k^2-4k+2}}$	0	$(1-k)\sqrt{\frac{1-P_0}{3k^2-4k+2}}$	$(1-k)(3k-1) < P_0 \leq \frac{2(1-k^2)}{(2-k)^2}$
	0	$\frac{1}{2}-\frac{k}{2}\sqrt{\frac{1-P_0}{3k^2-4k+2}}$	$\frac{1}{2}+\frac{k-2}{2}\sqrt{\frac{1-P_0}{3k^2-4k+2}}$	$(1-k)\sqrt{\frac{1-P_0}{3k^2-4k+2}}$	$\frac{2(1-k^2)}{(2-k)^2} < P_0 \leq 1$
$k > 1$	$1-\sqrt{\frac{P_0}{2(k-1)}}$	$\sqrt{\frac{(k-1)P_0}{2}}$	$\sqrt{\frac{(k-1)P_0}{2}}$	$1-k\sqrt{\frac{P_0}{2(k-1)}}$	$0 < P_0 \leq \frac{2(k-1)}{k^2}$
	$(k-1)\sqrt{\frac{1-P_0}{k^2-2k+2}}$	$\frac{k-2}{2}\sqrt{\frac{1-P_0}{k^2-2k+2}}+\frac{1}{2}$	$\frac{k-2}{2}\sqrt{\frac{1-P_0}{k^2-2k+2}}+\frac{1}{2}$	0	$\frac{2(k-1)}{k^2} < P_0 \leq 1$

voltage, and x denotes the output signal of the proportional-integral (PI) controller. Above all, the ranges of the voltage conversion ratio k should be determined by detecting the input and output voltages. However, during the start-up, the initial output voltage is 0, and thus, the voltage conversion ratio k will be infinite. In order to avoid this impact, the output voltage V_2 is replaced by the reference value V_{2ref} in practice. Subsequently, the signal x is utilized to realize the optimal control under different power ranges. For instance, during $0 < k \leq 0.5$, it can be seen from Fig. 14 that D^* is monotonically decreased along with the transferred power P_0 during the entire power range. Therefore, D^* is expressed by $1-x$ to realize the closed-loop control. According to the relationships among the optimal control variables as shown in (16), (19), and (21), the other three control variables D_1^*, D_2^* and D_0^* can be obtained. Furthermore, the boundaries of x should be addressed corresponding to the power boundaries. For the two power boundaries during $0 < k \leq 0.5$ as shown in (23), the corresponding values of D^* can be calculated as $D^* = 1-k$ and $D^* = (1-k)/(1+k)$ at the two power boundaries. Therefore, the two boundaries of x can be obtained as $x = k$ and $x = 2k/(1+k)$ due to $D^* = 1-x$. With a similar analysis, the closed-loop control system during $0.5 < k \leq 1$ and $k > 1$ can be obtained.

In conclusion, the expressions of the control variables can be simplified compared to the original expressions shown in Table IV. In addition, the ranges of the signal x can indicate the power ranges, which means the load-current sensor for detecting the transferred power is not required. Therefore, the hardware cost and the modulation complexity can be reduced by employing this closed-loop control system.

C. Current Stress Comparison Among Various Strategies

In addition to the five-level control strategy, the MCS modulation have also been discussed based on other multi-phase-shift control strategies, e.g., EPS, DPS, and TPS control. It has been verified that among these multi-phase-shift control strategies, the optimal modulation scheme based on TPS control can achieve the best performance, e.g., minimum current stress, and highest efficiency [2], [26]. Thus, the comparison of the peak current under TPS control, traditional SPS control, and five-level control are performed. The waveforms of the voltages and inductor current, and the control variables under SPS and TPS control are given in Fig. 18. With a similar optimal process, the optimal solutions for the MCS modulation under the SPS and TPS control are obtained as shown in Table V. Furthermore, the current stress with the SPS control, TPS control, and five-level control can be obtained based on the optimal solutions and peak current expressions, as shown in Table VI, where the power ranges correspond to those in Tables IV and V. It can be seen from Table VI that during $k > 1$, the peak current with the TPS control and five-level control strategies is identical. The comparison of the current stress with various control strategies is illustrated in Fig. 19, where it can be seen that the MCS modulation with the five-level control can achieve the lowest current stress during the whole power range under various k.

TABLE V
MCS SOLUTIONS WITH SPS AND TPS CONTROL STRATEGIES

Control	Ranges of k	Optimal control variables	Power ranges
SPS	whole	$D_0^* = \frac{1-\sqrt{1-P_0}}{2}$	$0 < P_0 \leq 1$
TPS	$k \leq 1$	$D_1^* = 1-\sqrt{\frac{P_0}{2k(k-1)}}$ $D_0^* = 0, D_2^* = kD_1^* - k + 1$	$0 < P_0 \leq 2(k-k^2)$
		$D_0^* = \frac{1}{2}(1-\sqrt{\frac{1-P_0}{2k^2-2k+1}})$ $D_1^* = 0, D_2^* = (2k-1)D_0^* - k + 1$	$2(k-k^2) < P_0 \leq 1$
	$k > 1$	$D_1^* = 1-\sqrt{\frac{P_0}{2(k-1)}}$ $D_0^* = (k-1)(1-D_1^*), D_2^* = D_1^*$	$0 < P_0 \leq \frac{2(k-1)}{k^2}$
		$D_1^* = (k-1)\sqrt{\frac{1-P_0}{k^2-2k+2}}$ $D_0^* = D_2^* = \frac{k-2}{2k-2}D_1^* + \frac{1}{2}$	$\frac{2(k-1)}{k^2} < P_0 \leq 1$

D. ZVS Discussion

To investigate the ZVS regions of the 2/3-level DAB converter under the proposed control strategy, the ZVS constraints of all switches should be explored. In order to achieve ZVS operation, the inductor current should be larger than a certain

TABLE VI
CURRENT STRESS COMPARISON AMONG VARIOUS STRATEGIES

Strategies	Ranges of k	Power ranges	Current stress i_0
SPS	$k \le 1$	whole	$2(1-k\sqrt{1-P_0})$
	$k > 1$	whole	$2(k-\sqrt{1-P_0})$
TPS	$k \le 1$	low	$2\sqrt{2k(1-k)P_0}$
		high	$2(1-\sqrt{(2k^2-2k+1)(1-P_0)})$
	$k > 1$	low	$2\sqrt{2(k-1)P_0}$
		high	$2(k-\sqrt{(k^2-2k+2)(1-P_0)})$
Five-level	$k \le 0.5$	low	$2\sqrt{k(2-3k)P_0}$
		medium	$2(1-\sqrt{(3k^2-2k+1)(1-P_0)})$
		high	$2(1-\sqrt{(3k^2-2k+1)(1-P_0)})$
	$0.5 < k \le 1$	low	$2\sqrt{(-3k^2+4k-1)P_0}$
		medium	$2(1-\sqrt{(3k^2-4k+2)(1-P_0)})$
		high	$2(1-\sqrt{(3k^2-4k+2)(1-P_0)})$
	$k > 1$	low	$2\sqrt{2(k-1)P_0}$
		high	$2(k-\sqrt{(2k^2-2k+2)(1-P_0)})$

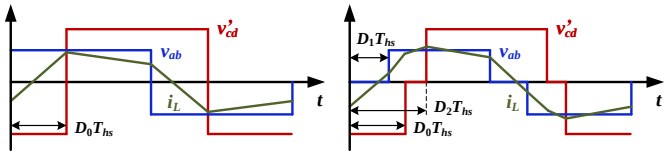

(a) (b)

Fig. 18. Typical waveforms with: (a) SPS control, and (b) TPS control.

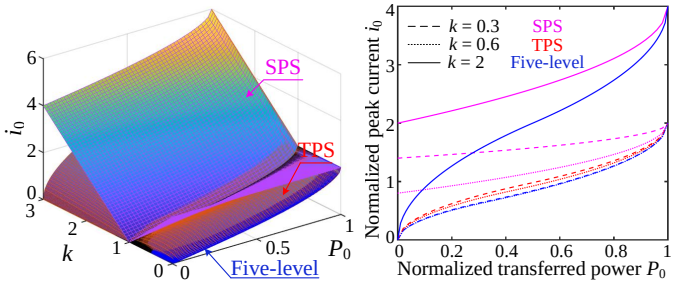

(a) (b)

Fig. 19. Current stress comparison with different control strategies: (a) 3-D comparison with various k and P_0. (b) 2-D comparison with various P_0 under fixed k.

value to ensure the parasitic capacitors of the switches can be fully discharged before the switches are turned on, i.e.,

$$\begin{cases} \frac{1}{2}L_s I_{L1}^2 > 2\cdot\frac{1}{2}C_p V_1^2, & \text{primary side} \\ \frac{1}{2}L_s I_{L2}^2 > 4\cdot\frac{1}{2}C_p(\frac{V_2}{2})^2, & \text{secondary side} \end{cases} \tag{24}$$

where I_{L1} and I_{L2} are the inductor currents at the switching instance, and C_p is the parasitic capacitance of the switches [30]. Therefore, the ZVS constraints for various switches can be obtained as

$$\begin{cases} \mathrm{S}_{11}\&\mathrm{S}_{12} : i_L(t=0) < -\sqrt{2C_pV_1^2/L_s} \\ \mathrm{S}_{13}\&\mathrm{S}_{14} : i_L(t=D_1T_{hs}) < -\sqrt{2C_pV_1^2/L_s} \\ \mathrm{S}_{21}\&\mathrm{S}_{24} : i_L(t=(D_0+D)T_{hs}) > \sqrt{C_pV_2^2/L_s} \\ \mathrm{S}_{22}\&\mathrm{S}_{23} : i_L(t=D_0T_{hs}) > \sqrt{C_pV_2^2/L_s} \\ \mathrm{S}_{26}\&\mathrm{S}_{27} : i_L(t=D_2T_{hs}) > \sqrt{C_pV_2^2/L_s} \\ \mathrm{S}_{25}\&\mathrm{S}_{28} : i_L(t=(D_2+D)T_{hs}) > \sqrt{C_pV_2^2/L_s} \end{cases} \tag{25}$$

The inductor current at the switching instance can be calculated according to (4) and the control variables (as shown in Table IV). For instance, under the condition $0 < k \le 0.5$ and $2k(2-k)/(k+1)^2 < P_0 \le 1$, the inductor current can be obtained as

$$\begin{cases} i_L(t=0) = i_L(t=D_1T_{hs}) = \frac{T_{hs}V_2}{2nL_s}\cdot(kM-k) \\ i_L(t=(D_0+D)T_{hs}) = \frac{T_{hs}V_2}{2nL_s}\cdot((-3k^2+2k-1)M+1) \\ i_L(t=D_0T_{hs}) = \frac{T_{hs}V_2}{2nL_s}\cdot(-(k^2+k+1)M+1) \\ i_L(t=D_2T_{hs}) = \frac{T_{hs}V_2}{2nL_s}\cdot((k^2-1)M+1) \\ i_L(t=(D_2+D)T_{hs}) = \frac{T_{hs}V_2}{2nL_s}\cdot((-k^2+k-1)M+1) \\ M = \sqrt{\frac{1-P_0}{3k^2-2k+1}} \end{cases} \tag{26}$$

Combining (25) and (26), the ZVS constraints for all switches under the condition $0 < k \le 0.5$ and $2k(2-k)/(k+1)^2 < P_0 \le 1$ can be verified, and then, the ZVS conditions can be obtained as: 1) during $2k(2-k)/(k+1)^2 < P_0 \le 1-(3k^2-2k+1)/(k^2+k+1)^2$, the ZVS constraint for S_{22} and S_{23} in (25) cannot be fulfilled, and thus, S_{22} and S_{23} cannot operate in ZVS, while the other switches can work in ZVS since their ZVS constraints can be fulfilled; 2) during $1-(3k^2-2k+1)/(k^2+k+1)^2 < P_0 \le 1$, all switches can operate in ZVS. In a similar way, the ZVS constraints for all operating conditions under the proposed control strategy can be obtained, as summarized in Table VII.

As the main aim of this paper is to propose a generic and simplified control strategy for the applications where the operating conditions/parameters vary in a wide range, the ZVS constraints are not considered during the optimization. That is because it will be very challenging to obtain the analytical solutions if both the ZVS and minimum current stress are applied as the optimization objectives for the multi-level DAB converters with five-level control (i.e., increased number of control variables and more complex constraints). As is to say, the efficiency of the DAB converter and control complexity are compromised in the proposed modulation strategy to suit the applications where the operating parameters vary in a wide range. If the two optimization objectives are required to be achieved for the multi-level DAB converters in certain

TABLE VII
ZVS CONDITIONS FOR ALL OPERATING CONDITIONS UNDER THE PROPOSED CONTROL STRATEGY

Ranges of k	Ranges of P_0	ZVS conditions
$0 < k \leq 0.5$	$0 < P_0 \leq 1 - \frac{4(3k^2-2k+1)}{(k+2)^2}$	S_{13}, S_{14}, S_{22}, and S_{23} operate in non-ZVS; the others operate in ZVS
	$1 - \frac{4(3k^2-2k+1)}{(k+2)^2} < P_0 \leq 1 - \frac{3k^2-2k+1}{(k^2+k+1)^2}$	S_{22} and S_{23} operate in non-ZVS; the others operate in ZVS
	$1 - \frac{3k^2-2k+1}{(k^2+k+1)^2} < P_0 \leq 1$	all switches operate in ZVS
$0.5 < k \leq 1$	$0 < P_0 \leq \frac{-11k^2+10k+1}{(3-k)^2}$	S_{13}, S_{14}, S_{22}, and S_{23} operate in non-ZVS; the others operate in ZVS
	$\frac{-11k^2+10k+1}{(3-k)^2} < P_0 \leq \frac{2(1-k^2)}{(2-k)^2}$	S_{22} and S_{23} operate in non-ZVS; the others operate in ZVS
	$\frac{2(1-k^2)}{(2-k)^2} < P_0 \leq 1$	all switches operate in ZVS
$k > 1$	$0 < P_0 \leq \frac{2(k-1)}{k^2}$	S_{13}, S_{14}, $S_{21}-S_{28}$ operate in non-ZVS; the others operate in ZVS
	$\frac{2(k-1)}{k^2} < P_0 \leq 1$	all switches operate in ZVS

TABLE VIII
MAIN PARAMETERS OF THE EXPERIMENTS

Parameters	Values
Rated power P	2.5 kW
Transformer turns ratio n	2
Series inductor L_s	100 μH
Input DC-link capacitors C_1	680 μF
Output DC-link capacitors C_2, C_3	680 μF
Switching frequency f	10 kHz
Power switches (IGBT)	Semikron SK35GB12T4

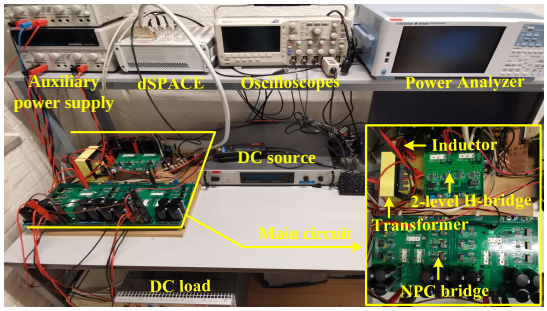

Fig. 20. Experimental setup of a 2/3-level DAB converter.

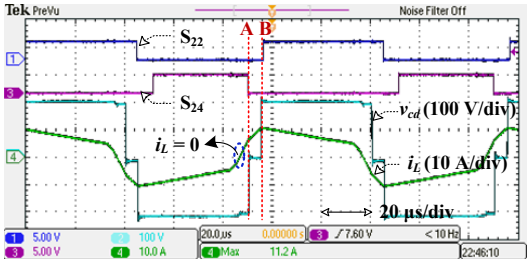

(a)

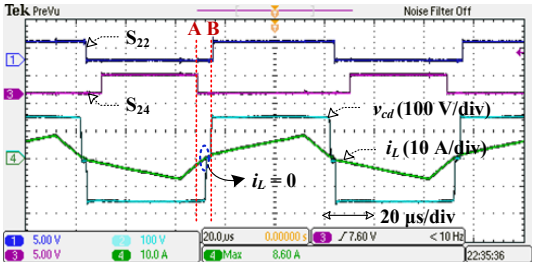

(b)

Fig. 21. Experimental waveforms by using the modulation scheme proposed in [7] under the condition V_1 = 100 V, R = 78 Ω and: (a) D_1 = 0.05, D_0 = 0.15, D = 0.2. (b) D_1 = 0.2, D_0 = 0.15, D = 0.2.

applications, there are two potential solutions, i.e., 1) the numerical solutions can be pre-calculated and then stored in a look-up table in microcontrollers. However, this method is mainly suitable for the applications where the operating parameters vary in a limited range; 2) the curve fitting can be used to obtain the analytical solutions based on the numerical solutions. Yet, the accuracy of the optimum control may be affected with the fitting curves. The above is of interest to further improve the efficiency of the 2/3-level DAB converter.

V. EXPERIMENTAL RESULTS

To validate the above analysis and the effectiveness of the proposed MCS control scheme, a hardware setup is developed as shown in Fig. 20, which is controlled by a dSPACE MicroLabBox. The main parameters of the prototype are shown in Table VIII.

A. Operating Constraints Verification

Fig. 21 shows the experimental results for the example in [7], whose switching sequence was shown in Fig. 3 (a). According to the aforementioned analysis, during the interval [A, B], the switching state fails to meet the universal operating constraint. Therefore, we mainly focus on the performance of the DAB converter during this interval. In Fig. 21 (a), the input voltage is 100 V, the DC load is 78 Ω, and the control variables are: D_1 = 0.05, D_0 = 0.15, and D = 0.2 (three control variables are employed in this modulation). As shown in Fig. 21 (a), the zero-crossing point of the inductor current i_L occurs before point A. In this condition, the voltage v_{cd} changes from $-V_2$ to $-0.5V_2$ at the falling edge of the gate-driving signal for S_{24} (i.e., point A). Therefore, the voltage waveform is only determined by the switching sequence without being affected by the zero-crossing point of the inductor current. On the

other hand, in Fig. 21 (b), the primary-side inner phase-shift ratio D_1 increases to 0.2, and the secondary-side switching sequence keeps constant. In this condition, the zero-crossing point changes along with the transferred power, and occurs during the interval [A, B]. As a result, the voltage v_{cd} changes from $-V_2$ to $-0.5V_2$ at the zero-crossing point instead of point A, which means the voltage waveform is affected by the current polarity. This example indicates that, since the switching state fails to satisfy the universal operating constraint, the waveforms may be affected by the inductor current polarity although with the same secondary-side switching sequence. As a result, the operating state analysis and power modeling will be very complex. Therefore, the proposed operating constraint should be satisfied to decouple the voltage waveform from the current polarity in practice.

Another example indicating the operating constraint $D_2 + D \leq 1+D_0$ (i.e., Eq. (3)) is shown in Fig. 22, where the input voltage is 150 V, the output voltage is 300 V, and the DC load is 115 Ω. In Fig. 22 (a), the control variables are D_1 = 0.25, D_2 = 0.15, D_0 = 0.1, and D = 0.25 ($D_2+D \leq 1+D_0$ is satisfied). It can be seen from Fig. 22 (a) that the waveform of the voltage v_{cd} is five-level. On the other hand, when $D_2 + D > 1 + D_0$, the experimental waveforms are shown in Fig. 22 (b), where D_1 = 0.25, D_2 = 0.5, D_0 = 0.1, and D = 0.7. As shown in Fig. 22 (b), the waveform of the voltage v_{cd} becomes three-level, whose highest voltage levels $\pm V_2$ are replaced by 0, which corresponds to the theoretical analysis in Section II. In addition, the peak current increases from 9.4 A in Fig. 22 (a) to 27 A in Fig. 22 (b), which means the current stress under the condition $D_2 + D > 1 + D_0$ will be significantly increased with the same transferred power. Furthermore, the power modeling is different between the three-level voltage and five-level voltage. Therefore, in order to improve the performances, such as reducing the current stress, and simplify the modeling, the operating constraint $D_2+D \leq 1+D_0$ should be satisfied.

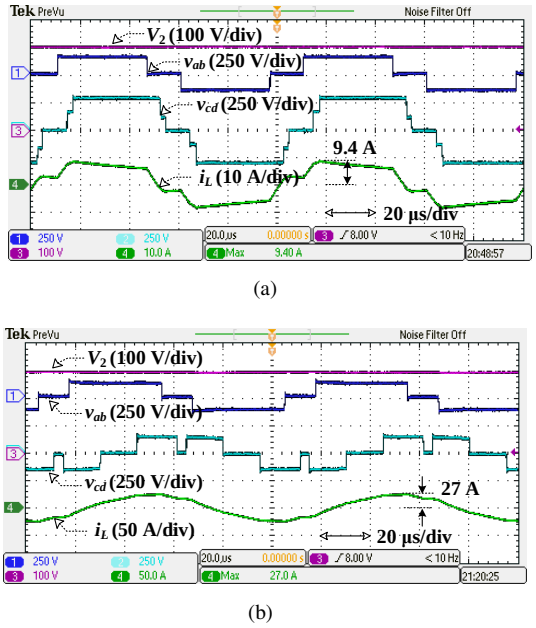

Fig. 22. Experimental waveforms with the five-level control scheme under the condition V_1 = 150 V, V_2 = 300 V, R = 115 Ω and: (a) D_1 = 0.25, D_2 = 0.15, D_0 = 0.1, D = 0.25. (b) D_1 = 0.25, D_2 = 0.5, D_0 = 0.1, D = 0.7.

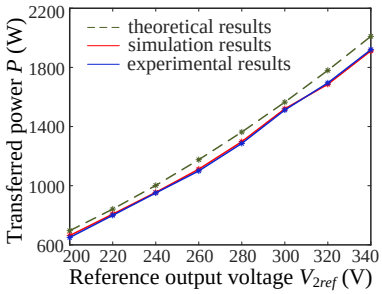

Fig. 23. Comparative curves of the transferred power among theoretical, simulation, and experimental results.

B. Modeling Accuracy

In order to verify the accuracy of the obtained power model, simulation (by PLECS) and experimental tests have been performed with an open-loop control system to compare with the theoretical results, as shown in Fig. 23, where the input voltage is 150 V, the output load is 57.5 Ω, and the reference output voltage (e.g., theoretical output voltage) changes from 200 V to 340 V. It can be seen from Fig. 23 that the simulation and experimental results are well aligned, and also close to the theoretical results. The difference between the theoretical results and the experimental results mainly caused by the power losses, which are not considered during the modeling process. The power losses were also not considered in the traditional power modeling methods [25]–[27], unless power losses are the optimization objective. Note that the transferred power models obtained by using the equivalent-wave method are the same as the power models by using the traditional piecewise integration method. However, the modeling can be simplified by using the equivalent-wave method.

C. Current Stress and Efficiency Comparison

To validate the performance of the proposed MCS control scheme, experimental tests under various control strategies are performed, i.e., SPS control, MCS modulation based on TPS (MCS-TPS) control, Five-level control in [31], and the proposed MCS modulation based on five-level (MCS-Five-level) control. Figs. 24 and 25 show the experimental waveforms with the above four control strategies. In Fig. 24, the input voltage is 70 V, the output voltage is 300 V (i.e., k = 0.47), and the transferred power is 580 W. It can be seen from Fig. 24 that the peak current can be reduced from 28.4 A with the SPS control to 18.8 A with the MCS-TPS control and 18.4 A with the Five-level control in [31], and further to 16.4 A with the proposed MCS-Five-level control. Meanwhile, the efficiency of the 2/3-level DAB converter can be increased from 84.5% with SPS control to 90.8% with the proposed control strategy. On the other hand, the input voltage is 200 V, the output voltage is 300 V (i.e., k = 1.33), and the transferred power increases to 1153 W in Fig. 25. It can be seen from Fig. 25 that the experimental waveforms, the peak current, and

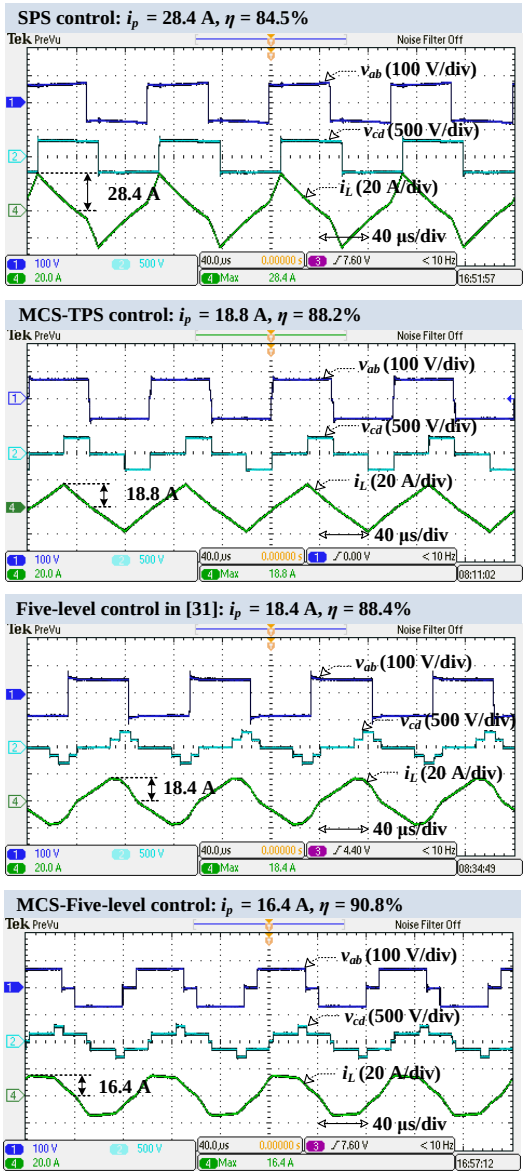

Fig. 24. Experimental waveforms of the 2/3-level DAB converter with various modulation schemes under V_1 = 70 V, V_2 = 300 V, and P = 580 W.

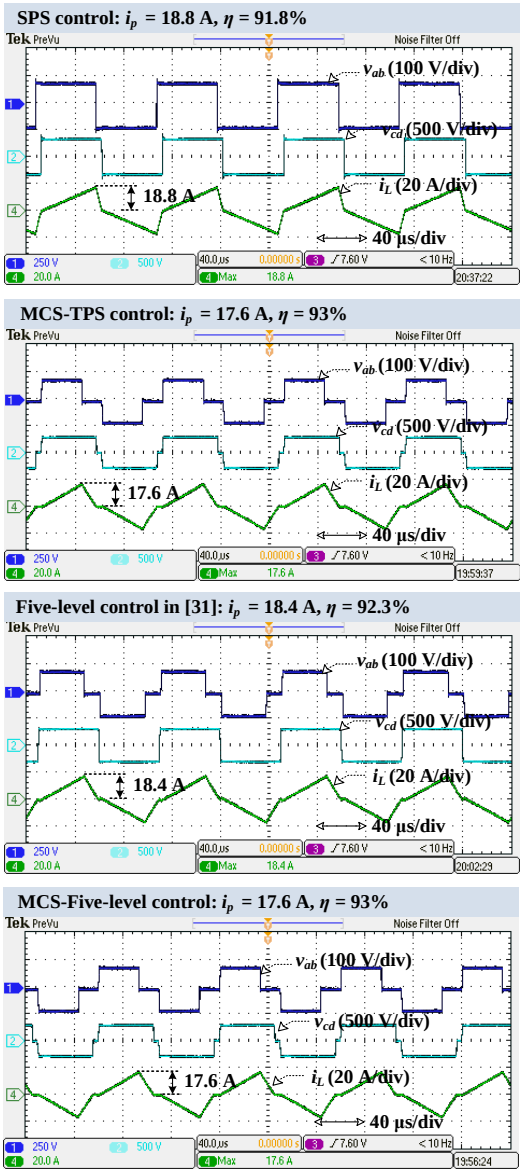

Fig. 25. Experimental waveforms of the 2/3-level DAB converter with various modulation schemes under V_1 = 200 V, V_2 = 300 V, and P = 1153 W.

the efficiency are identical by applying the MCS-TPS control and the proposed MCS control strategy, which corresponds to the theoretical analysis about the current stress comparison during $k > 1$ in Section IV. Moreover, the peak current with the proposed strategy can be reduced compared to the SPS control and the Five-level control in [31], and the efficiency can be increased at the same time.

Furthermore, the power losses distribution with various control strategies under V_1 = 70 V, V_2 = 300 V, and P = 580 W is shown in Fig. 26, where it can be seen that with the reduced current stress, various power losses including conduction, switching, and magnetic losses (the losses on the transformer and the auxiliary inductor) will be reduced with the proposed MCS-Five-level control strategy.

The experimental curves of the peak current with respect to the transferred power with various control strategies are shown in Fig. 27, where NS denotes the modulation strategy with

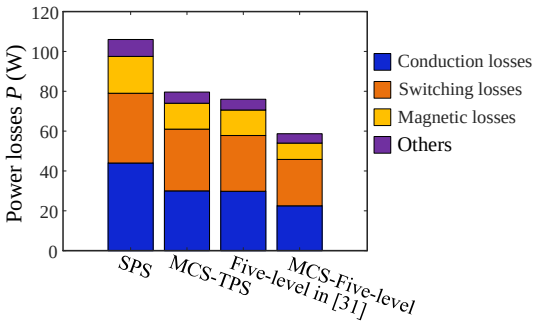

Fig. 26. Power loss distribution with various modulation schemes under V_1 = 70 V, V_2 = 300 V, and P = 580 W, which is obtained by simulation in PLECS.

optimal numerical solutions obtained by using Mathematica. Under different voltage conversion ratio k, the proposed MCS-

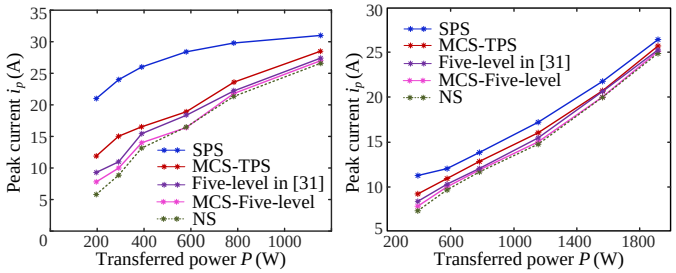

Fig. 27. Peak current curves of the DAB converters with varying power under: (a) V_1 = 70 V, and V_2 = 300 V. (b) V_1 = 120 V, and V_2 = 300 V.

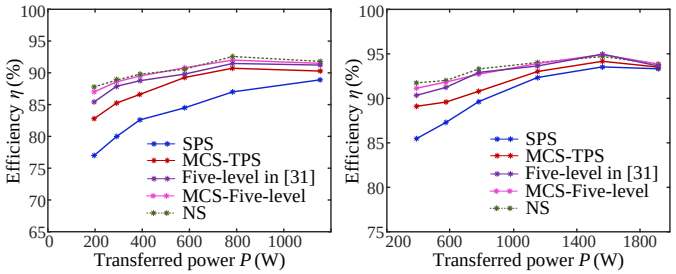

Fig. 28. Efficiency curves of the DAB converters with varying power under: (a) V_1 = 70 V, and V_2 = 300 V. (b) V_1 = 120 V, and V_2 = 300 V.

Five-level control strategy can achieve the lowest current stress during the entire power range compared to the SPS control, MCS-TPS control, and the Five-level control in [31]. Meanwhile, the efficiency of the DAB converter can also be improved by applying the proposed strategy, as shown in Fig. 28. In addition, the performance (i.e., current stress and efficiency) of the proposed MCS-Five-level control strategy is similar to that of the NS control strategy. However, this strategy and the Five-level control in [31] are based on numerical solutions, which depend on pre-calculation of the control variables offline, and if the operating parameters (e.g., DC-link voltages) change, the optimal solutions should be re-calculated and then updated to a look-up table in the microcontroller. Compared to them, the proposed control strategy based on analytical solutions can achieve similar performance with numerical solutions, while simplifying the control complexity significantly, especially when the DC-link voltages and transferred power change in a wide range.

Furthermore, the comparative experimental results with various control strategies under different voltage conversion ratio k are shown in Fig. 29, where the output voltage V_2 is 300 V, the transferred power P is 1000 W, and the input voltage V_1 changes from 70 V to 210 V, i.e., the voltage conversion ratio k changes from 0.46 to 1.4. As shown in Fig. 29, the proposed MCS control strategy can minimize the current stress and improve the efficiency under various voltage conversion ratios, especially when k is away from unity (V_1 = 150 V).

D. Dynamics of the Proposed Closed-Loop Control

In the proposed closed-loop control system (i.e., Fig. 17), the relationships between the control variables and the output signal of the PI controller (i.e., x) will change during different power ranges. Therefore, it is crucial to ensure smooth transition during the transferred power changes, especially between light-load and heavy-load transition. Fig. 30 illustrates the dynamics when the transferred power changes between 577 W and 1363 W (i.e., the DC load changes between 156 Ω and 66 Ω), where the input voltage is 120 V and the output voltage is 300 V. It can be seen from Fig. 30 that by applying the proposed closed-loop control scheme, the 2/3-level DAB converters can change the transferred power between light load and heavy load seamlessly.

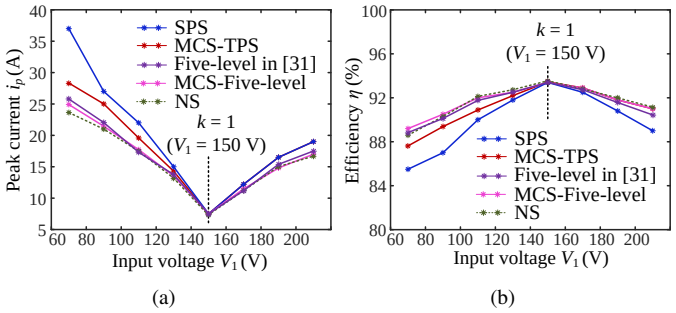

Fig. 29. Comparison curves with different input voltages under the condition V_2 = 300 V and P = 1000 W. (a) Peak current curves. (b) Efficiency curves.

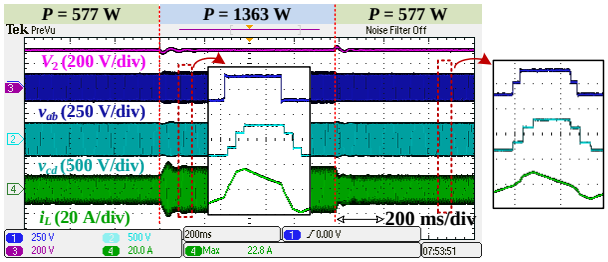

Fig. 30. Dynamic waveforms by applying the proposed closed-loop control scheme with step changes in the transferred power.

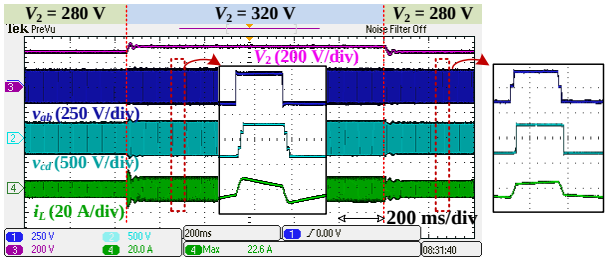

Fig. 31. Dynamic waveforms by applying the proposed closed-loop control scheme with step changes in the output voltage.

In addition, during different ranges of the voltage conversion ratio k, the analytical solutions will also be different. Thus, reliable transition between different voltage conversion ratios should also be realized. Fig. 31 illustrates the dynamics of the proposed method when a step change in the output voltage from 280 V to 320 V is applied, i.e., the voltage conversion

ration k changes from 1.07 to 0.94, while the input voltage remains at 150 V. Although the control variables are expressed differently under the conditions $k \leq 1$ and $k > 1$, the transition between the two conditions can be completed smoothly with the proposed closed-loop control system.

VI. Conclusion

This paper has discussed the modulation scheme for the 2/3-level DAB converters comprehensively. Accordingly, the operating constraints have been revealed to ensure stable and reliable operation of the DAB converters without voltage distortions. Subsequently, the transferred power and current stress models have been developed by utilizing the equivalent-wave method to simplify the modeling and reduce the computation burdens. Based on the developed models, a generic optimal modulation scheme has been proposed to minimize the current stress and improve the efficiency. The analytical solutions, obtained by using the KKT conditions and numerical-solution analysis, were employed in the proposed modulation scheme. Furthermore, a simplified closed-loop control system has been designed, which enables online regulation for the optimal control variables when the operating conditions change. With the proposed control strategy, current sensor is not required to determine the transferred power. Therefore, the hardware cost and control complexity can be reduced. Extensive experimental tests have verified that the current stress of the 2/3-level DAB converters can be reduced by the proposed MCS control scheme, along with a higher efficiency over the entire power range and various voltage conversion ratios.

References

[1] R. W. De Doncker, D. M. Divan, and M. H. Kheraluwala, "A Three-Phase Soft-Switched High-Power-Density DC/DC Converter for High-Power Applications," *IEEE Trans. Ind. Appl*., vol. 27, no. 1, pp. 63-73, Jan.-Feb. 1991.

[2] N. Hou and Y. W. Li, "Overview and Comparison of Modulation and Control Strategies for a Nonresonant Single-Phase Dual-Active-Bridge DC–DC Converter," *IEEE Trans. Power Electron*., vol. 35, no. 3, pp. 3148-3172, Mar. 2020.

[3] B. Zhao, Q. Song, W. Liu, and Y. Sun, "Overview of Dual-Active-Bridge Isolated Bidirectional DC–DC Converter for High-Frequency-Link Power-Conversion System," *IEEE Trans. Power Electron*., vol. 29, no. 8, pp. 4091-4106, Aug. 2014.

[4] Z. Wang and H. Li, "A Soft Switching Three-phase Current-fed Bidirectional DC-DC Converter With High Efficiency Over a Wide Input Voltage Range," *IEEE Trans. Power Electron*., vol. 27, no. 2, pp. 669-684, Feb. 2012.

[5] H. Choi, B. Seo, M. Ryu, Y. Cho, and J. Jung, "Effective Magnetic Component Design of Three-Phase Dual-Active-Bridge Converter for LVDC Distribution System," *IEEE Trans. Ind. Electron*., vol. 68, no. 3, pp. 1828-1840, Mar. 2021.

[6] M. A. Moonem and H. Krishnaswami, "Analysis and Control of Multi-Level Dual Active Bridge DC-DC Converter," in *Proc. ECCE*, Raleigh, NC, 2012, pp. 1556-1561.

[7] M. A. Awal, M. R. Bipu, O. A. Montes, H. Feng, I. Husain, W. Yu, and S. Lukic, "Capacitor Voltage Balancing for Neutral Point Clamped Dual Active Bridge Converters," *IEEE Trans. Power Electron*., vol. 35, no. 10, pp. 11267-11276, Oct. 2020.

[8] P. Liu, C. Chen, S. Duan, and W. Zhu, "Dual Phase-Shifted Modulation Strategy for the Three-Level Dual Active Bridge DC–DC Converter," *IEEE Trans. Ind. Electron*., vol. 64, no. 10, pp. 7819-7830, Oct. 2017.

[9] A. Filba-Martinez, S. Busquets-Monge, J. Nicolas-Apruzzese, and J. Bordonau, "Operating Principle and Performance Optimization of a Three-Level NPC Dual-Active-Bridge DC–DC Converter," *IEEE Trans. Ind. Electron*., vol. 63, no. 2, pp. 678-690, Feb. 2016.

[10] A. Filba-Martinez, S. Busquets-Monge, and J. Bordonau, "Modulation and Capacitor Voltage Balancing Control of Multilevel NPC Dual Active Bridge DC–DC Converters," *IEEE Trans. Ind. Electron*., vol. 67, no. 4, pp. 2499-2510, Apr. 2020.

[11] M. A. Moonem, T. Duman, and H. Krishnaswami, "Capacitor Voltage Balancing in a Neutral-Point Clamped Multilevel DC-DC Dual Active Bridge Converter," in *Proc. PEDG*, Florianopolis, 2017, pp. 1-7.

[12] C. Song, A. Sangwongwanich, Y. Yang, and F. Blaabjerg, "Capacitor Voltage Balancing for Multi-Level Dual-Active-Bridge DC-DC Converters," *IEEE Trans. Ind. Electron*., vol. 70, no. 3, pp. 2566-2575, Mar. 2023.

[13] Y. Shi, X. Wang, J. Xi, X. Gui, and X. Yang, "Wide Load Range ZVZCS Three-Level DC-DC Converter With Compact Structure," *IEEE Trans. Power Electron*., vol. 34, no. 6, pp. 5032-5037, June 2019.

[14] D. Liu, Y. Wang, Q. Zhang, and Z. Chen, "ZVZCS Full-Bridge Three-Level DC/DC Converter With Reduced Device Count," *IEEE Trans. Power Electron*., vol. 35, no. 10, pp. 9965-9970, Oct. 2020.

[15] Z. Guo and K. Sun, "Three-Level Bidirectional DC-DC Converter With an Auxiliary Inductor in Adaptive Working Mode for Full-Operation Zero-Voltage Switching," *IEEE Trans. Power Electron*., vol. 33, no. 10, pp. 8537-8552, Oct. 2018.

[16] G. Chen, Z. Chen, Y. Chen, C. Feng, and X. Zhu, "Asymmetric Phase-Shift Modulation Strategy of DAB Converters for Improved Light-Load Efficiency," *IEEE Trans. Power Electron*., vol. 37, no. 8, pp. 9104-9113, Aug. 2022.

[17] D. Mou, Q. Luo, Z. Wang, J. Li, Y. Wei, H. Shi, and X. Du, "Optimal Asymmetric Duty Modulation to Minimize Inductor Peak-to-Peak Current for Dual Active Bridge DC-DC Converter," *IEEE Trans. Power Electron*., vol. 36, no. 4, pp. 4572-4584, Apr. 2021.

[18] M. Mahdavifard, N. Mazloum, F. Zahin, A. KhakparvarYazdi, A. Abasian, and S. A. Khajehoddin, "An Asymmetrical DAB Converter Modulation and Control Systems to Extend the ZVS Range and Improve Efficiency," *IEEE Trans. Power Electron*., vol. 37, no. 10, pp. 12774-12792, Oct. 2022.

[19] A. Tong, L. Hang, G. Li, X. Jiang, and S. Gao, "Modeling and Analysis of a Dual-Active-Bridge-Isolated Bidirectional DC/DC Converter to Minimize RMS Current with Whole Operating Range," *IEEE Trans. Power Electron*., vol. 33, no. 6, pp. 5302-5316, Jun. 2018.

[20] B. Zhao, Q. Yu, and W. Sun, "Extended-Phase-Shift Control of Isolated Bidirectional DC–DC Converter for Power Distribution in Microgrid," *IEEE Trans. Power Electron*., vol. 27, no. 11, pp. 4667-4680, Nov. 2012.

[21] H. Wen, J. Li, H. Shi, Y. Hu, and Y. Yang, "Fault Diagnosis and Tolerant Control of Dual-Active-Bridge Converter with Triple-Phase-Shift Control for Bidirectional EV Charging Systems," *IEEE Trans. Transport. Electrific*., vol. 7, no. 1, pp. 287-303, Mar. 2021.

[22] B. Zhao, Q. Song, and W. Liu, "Efficiency Characterization and Optimization of Isolated Bidirectional DC–DC Converter Based on Dual-Phase-Shift Control for DC Distribution Application," *IEEE Trans. Power Electron*., vol. 28, no. 4, pp. 1711-1727, Apr. 2013.

[23] F. Krismer and J. W. Kolar, "Efficiency-Optimized High-Current Dual Active Bridge Converter for Automotive Applications," *IEEE Trans. Ind. Electron*., vol. 59, no. 7, pp. 2745-2760, Jul. 2012.

[24] D. Mou, Q. Luo, Z. Wang, J. Li, Y. Wei, H. Shi, X. Du, and H. Mantooth, "Hybrid Duty Modulation for Dual Active Bridge Converter to Minimize RMS Current and Extend Soft-Switching Range Using the Frequency Domain Analysis," *IEEE Trans. Power Electron*., vol. 36, no. 4, pp. 4738-4751, Apr. 2021.

[25] J. Huang, Y. Wang, Z. Li, and W. Lei, "Unified Triple-Phase-Shift Control to Minimize Current Stress and Achieve Full Soft-Switching of Isolated Bidirectional DC–DC Converter," *IEEE Trans. Ind. Electron*., vol. 63, no. 7, pp. 4169-4179, Jul. 2016.

[26] N. Hou, W. Song, and M. Wu, "Minimum-Current-Stress Scheme of Dual Active Bridge DC–DC Converter with Unified Phase-Shift Control," *IEEE Trans. Power Electron*., vol. 31, no. 12, pp. 8552-8561, Dec. 2016.

[27] O. M. Hebala, A. A. Aboushady, K. H. Ahmed, and I. Abdelsalam, "Generic Closed-Loop Controller for Power Regulation in Dual Active Bridge DC–DC Converter with Current Stress Minimization," *IEEE Trans. Ind. Electron*., vol. 66, no. 6, pp. 4468-4478, Jun. 2019.

[28] B. Liu, P. Davari, and F. Blaabjerg, "An Optimized Hybrid Modulation Scheme for Reducing Conduction Losses in Dual Active Bridge Converters," *IEEE J. Emerg. Sel. Topics Power Electron*., vol. 9, no. 1, pp. 921-936, Feb. 2021.

[29] Q. Gu, L. Yuan, J. Nie, J. Sun, and Z. Zhao, "Current Stress Minimization of Dual-Active-Bridge DC-DC Converter Within the Whole Operating Range," *IEEE J. Emerg. Sel. Topics Power Electron*., vol. 7, no. 1, pp. 129-142, Mar. 2019.

[30] Y. Wang, H. Wen, Y. Zhu, H. Shi, Q. Bu, Y. Hu, and Y. Yong, "Minimum-Current-Stress Scheme of Three-Level Dual-Active-Bridge DC–DC Converters With the Particle Swarm Optimization," *IEEE Trans. Transport. Electrific.*, vol. 7, no. 4, pp. 2067-2084, Dec. 2021.
[31] P. Liu, C. Chen, and S. Duan, "An Optimized Modulation Strategy for the Three-Level DAB Converter With Five Control Degrees of Freedom," *IEEE Trans. Ind. Electron.*, vol. 67, no. 1, pp. 254-264, Jan. 2020.
[32] C. Song, Y. Yang, A. Sangwongwanich, Y. Pan, and F. Blaabjerg, "Modeling and Analysis of 2/3-Level Dual-Active-Bridge DC-DC Converters with the Five-Level Control Scheme," in *Proc. APEC*, Phoenix, USA, 2021, pp. 1958-1963.
[33] C. Song, Y. Yang, A. Sangwongwanich, and F. Blaabjerg, "Open-Circuit Fault Analysis and Fault-Tolerant Control for 2/3-Level DAB Converters," in *Proc. ECCE-Asia*, Singapore, 2021, pp. 696-701.
[34] J. Lee, H. Choi, and J. Jung, "Three level NPC Dual Active Bridge Capacitor Voltage Balancing Switching Modulation," in *Proc. INTELEC*, Broadbeach, QLD, Australia, 2017, pp. 438-443.

Chaochao Song (S'21) received the B.S. degree in automation and M.S. degree in power electronics from Shandong University, Ji′nan, China, in 2016 and 2019, respectively. He is currently working toward the Ph.D. degree at Aalborg University, Aalborg, Denmark. He was a Visiting Researcher with Fraunhofer ISE, Freiburg, Germany from June to September, 2022.

His current research interests include multi-level converters and renewable power generation.

Ariya Sangwongwanich (S'15-M'19) received the M.Sc. and Ph.D. degree in energy engineering from Aalborg University, Denmark, in 2015 and 2018, respectively. He is currently working as an Assistant Professor at the Department of Energy Technology, Aalborg University, where he is a Vice-Leader of Photovoltaic Systems research program. His research interests include control of grid-connected converters, photovoltaic systems, reliability in power electronics, and multi-level converters.

He was a Visiting Researcher with RWTH Aachen, Aachen, Germany from September to December 2017. Dr. Sangwongwanich was the recipient of the Danish Academy of Natural Sciences′ Ph.D. Prize and the Spar Nord Foundation Research Award for his Ph.D. thesis in 2019.

Yongheng Yang (SM'17) received the B.Eng. degree in electrical engineering and automation from Northwestern Polytechnical University, China, in 2009 and the Ph.D. degree in energy technology (power electronics and drives) from Aalborg University, Denmark, in 2014.

He was a postgraduate student with Southeast University, China, from 2009 to 2011. In 2013, he was a Visiting Scholar at Texas A&M University, USA. During 2014-2020, he was with the Department of Energy Technology, Aalborg University, where he became a tenured Associate Professor in 2018. In January 2021, he joined Zhejiang University, China, as a ZJU100 Professor. His research focuses on the grid-integration of photovoltaic systems and control of power converters, in particular, the grid-forming control technologies.

Dr. Yang was the Chair of the IEEE Denmark Section (2019-2020). He is an Associate Editor for several IEEE Transactions. He was the recipient of the 2018 IET Renewable Power Generation Premium Award and was an Outstanding Reviewer for the IEEE TRANSACTIONS ON POWER ELECTRONICS in 2018. He was the recipient of the 2021 Richard M. Bass Outstanding Young Power Electronics Engineer Award from the IEEE Power Electronics Society (PELS) and the 2022 Isao Takahashi Power Electronics Award. In addition, he has received two IEEE Best Paper Awards. He has been included on the list of Highly Cited Chinese Researchers by Elsevier in 2022. He is currently the Secretary of the IEEE PELS Technical Committee on Sustainable Energy Systems and a Council Member of the China Power Supply Society.

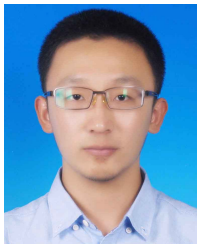

Yiwei Pan (S'19) received the B.S. degree in automation and M.S. degree in power electronics from Shandong University, Ji′nan, China, in 2015 and 2018, respectively, and the Ph.D. degree from Aalborg University, Aalborg, Denmark, in 2022. Since July 2022, he has been with Huawei, Shanghai, China, where he is currently an engineer with Digital Power Technology & Strategy Dept (Part of Huawei Digital Power Technologies).

He was an exchange student with Tianjin University, China from July 2016 to May 2018, and a Visiting Researcher with Kiel University, Germany from August to December 2021. His current research interests include multilevel converters and distributed power generation. He was the recipient of the Best Paper Award at IEEE IPEMC-ECCE Asia 2020, and the recipient of the Best Presentation Award at IEEE APEC 2021.

Frede Blaabjerg (S'86-M'88-SM'97-F'03) was with ABB-Scandia, Randers, Denmark, from 1987 to 1988. He got the Ph.D. degree in Electrical Engineering at Aalborg University in 1995. He became an Assistant Professor in 1992, an Associate Professor in 1996, and a Full Professor of power electronics and drives in 1998. From 2017 he became a Villum Investigator. He is honoris causa at University Politehnica Timisoara (UPT), Romania and Tallinn Technical University (TTU) in Estonia.

His current research interests include power electronics and its applications such as in wind turbines, PV systems, reliability, harmonics and adjustable speed drives. He has published more than 600 journal papers in the fields of power electronics. He is the co-author of four monographs and editor of ten books in power electronics and its applications.

He has received 33 IEEE Prize Paper Awards, the IEEE PELS Distinguished Service Award in 2009, the EPE-PEMC Council Award in 2010, the IEEE William E. Newell Power Electronics Award 2014, the Villum Kann Rasmussen Research Award 2014, the Global Energy Prize in 2019 and the 2020 IEEE Edison Medal. He was the Editor-in-Chief of the IEEE TRANSACTIONS ON POWER ELECTRONICS from 2006 to 2012. He has been Distinguished Lecturer for the IEEE Power Electronics Society from 2005 to 2007 and for the IEEE Industry Applications Society from 2010 to 2011 as well as 2017 to 2018. In 2019-2020 he serves as a President of IEEE Power Electronics Society. He has been Vice-President of the Danish Academy of Technical Sciences. He is nominated in 2014-2020 by Thomson Reuters to be between the most 250 cited researchers in Engineering in the world.